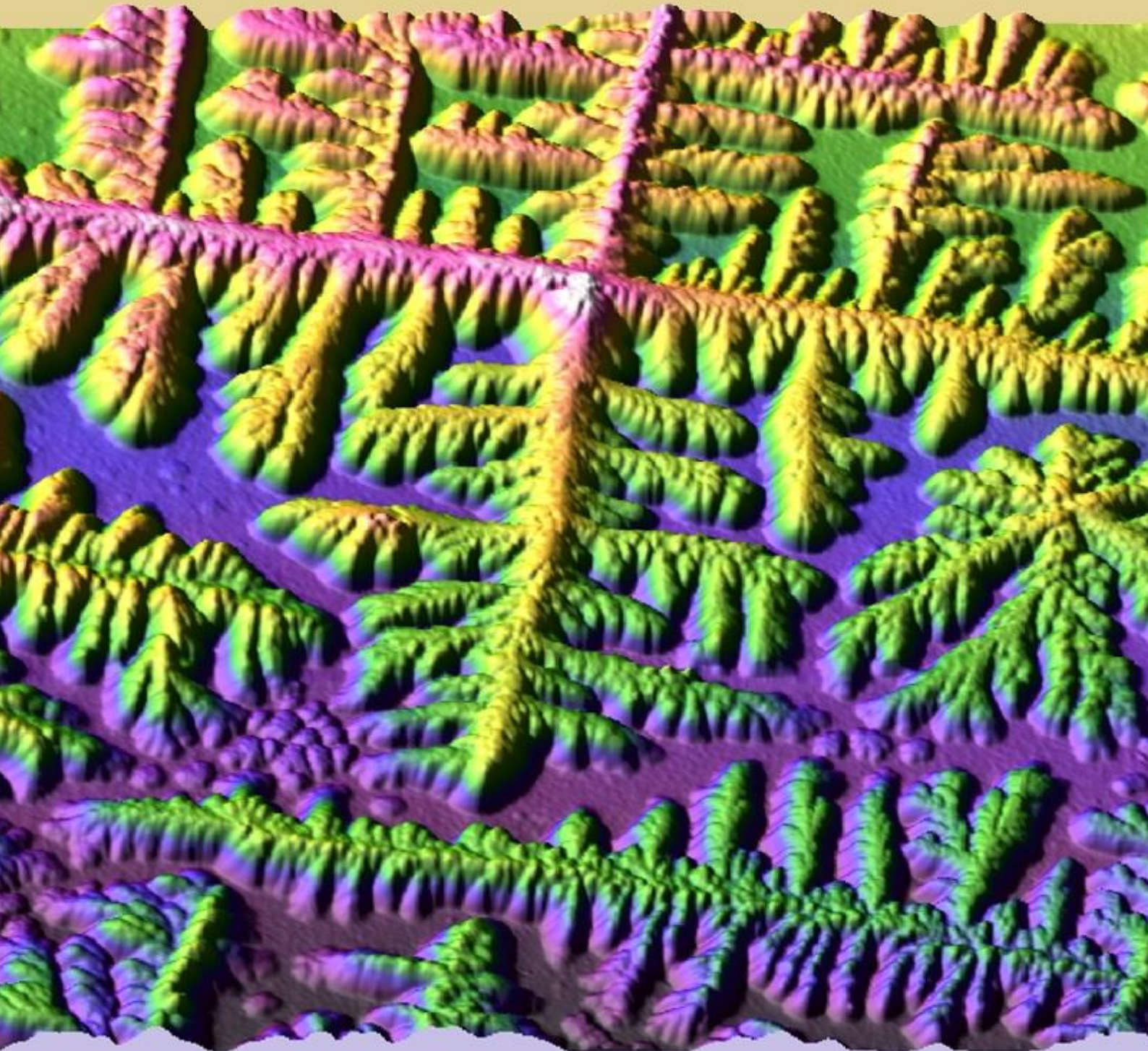


Volume 2, Number 1

March 2020

Nanomaterials Science & Engineering



Volume 2, Number 1

March 2020

Nanomaterials Science & Engineering

Title

Nanomaterials Science & Engineering (NMS&E), Vol.2, No.1, 2020

Editors-in-Chief

Igor Bdikin

Paula Alexandrina de Aguiar Pereira Marques

Duncan Paul Fagg

Editorial Board

Alexander Titov, Andrei Kovalevsky, António Manuel de Amaral Monteiro Ramos, António Manuel de Bastos Pereira, António Manuel Godinho Completo, Bagautdinov Bagautdin, Binay Kumar, Budhendra Singh, Cicero R. Cena, D. Pukazhselvan, Dmitry A. Kiselev, Dmitry Karpinsky, Eudes Borges de Araujo, Gil Gonçalves, Gonzalo Guillermo Otero Irurueta, Indrani Coondoo, João Paulo Davim Tavares da Silva, José Coutinho, Maciej Wojtas, Manoj Kumar Singh, Margarida Isabel Cabrita Marques Coelho, Maxim Silibin, Münir Tasdemir, Neeraj Panwar, Nikolai Sobolev, Oleksandr Tkach, Paula Celeste da Silva Ferreira, Philip Leduc, Radheshyam Rai, Sergey Bozhko, Svitlana Kopyl, Vincent Ball, Vítor António Ferreira da Costa, Vladimir Bystrov, Yuri Dekhtyar

Editorial Managers

Igor Bdikin

Gil Gonçalves

Raul Simões

Cover and Logo

Igor Bdikin (DNA microstructure, AFM image, 125x125x5 μm^3)

Publisher

University of Aveiro

Support

Serviços de Biblioteca, Informação Documental e Museologia

Centre for Mechanical Technology & Automation (TEMA)

Mechanical Engineering Department

University of Aveiro

Copyright Information

All work licensed under Creative Commons Attribution License that allows others to share the work with an acknowledgement of the work's authorship and initial publication in this journal. Copyrights to illustrations published in the journal remain with their current copyright holders. It is the author's responsibility to obtain permission to quote from copyright sources.

Mailing Address

Department of Mechanical Engineering

University of Aveiro

Aveiro 3810-193

Portugal

E-mail: bdikin@ua.pt

ISSN: 2184-7002

Georgiy Shakhgildyan, Maxim Vetchinnikov, Alexey Lipatiev, Sergey Lotarev, Vladimir Sigaev Femtosecond laser processing of Ag/CdS doped oxide glasses	5-10
V. S. Bystrov, I. K. Bdikin and Budhendra Singh Piezoelectric and ferroelectric properties of various amino acids and tubular dipeptide nanostructures: Molecular modelling	11-24
Saulo Portes dos Reis, Fernando Brondani Minussi and Eudes B. Araújo Thermally activated processes and bias field effects on the electrical properties of BiFeO₃ thin films	25-34
Nimisha Kaippamangalath, Unnikrishnan Gopalakrishnanpanicker, Praveen C. Ramamurthy Mechanical and Solvent Transport Characteristics of Nitro and n-Butylphenyl Supported Poly(1,3,4-Oxadiazole)s	35-43
Mohamed Ahmed ESHAG, Musaab ZAROG Sizing Electrode and its effect on performance of a microactuator	44-48
S.Guretsky, D.Karpinsky, I.Kolesova, A.Kravtsov, D.Zhaludkevich, S. Ozcelik, O.Dernovich, N.Kuleshov Growth and spectral characteristics of single crystal layer of KY(WO₄)₂ doped with Ho³⁺ ions	49-52

Femtosecond laser processing of Ag/CdS doped oxide glasses

**Georgiy Shakhgildyan*, Maxim Vetchinnikov, Alexey Lipatiev,
Sergey Lotarev, Vladimir Sigaev**

Mendeleev University of Chemical Technology of Russia, 9 Miusskaya sq., Moscow, Russia

**Corresponding authors, e-mail address: gshah@muctr.ru*

Received 16 October 2019; accepted 17 February 2020; published online 10 March 2020

ABSTRACT

Femtosecond laser processing (FLP) of oxide glasses doped with photosensitive agents (noble metals and semiconductors) opens new routes for precise space-selective tuning of material properties and development of functional photonic devices including integrated waveguides, optical switches, and volume optical memory. In this study, we showed how FLP can be used for the spatially-selective formation of micron-sized photoluminescent domains in the bulk of Ag-doped phosphate and Ag/CdS-doped silicate glasses. Multiphoton ionization caused by FLP leads to local heating of glass in the focal point, which initiates the precipitation and growth of photoluminescent Ag nanoclusters and CdS quantum dots in the periphery of the domains. The photoluminescence intensity of the formed domains depends on the laser exposure parameters, such as pulse energy and number of pulses that can be used in the future for multilevel optical data recording.

1. INTRODUCTION

Glasses with noble metals and chalcogenide semiconductors are popular subject of numerous studies for applications in optics and photonics [1-4]. The main feature of these glasses is possibility of bulk precipitation of metal or semiconductor nanoparticles with different sizes which could dramatically change the optical properties of glass. It is possible to control size of nanoparticles both by varying dopant concentration and heat-treatment conditions i.e. temperature or duration.

In recent decades availability of high powered femtosecond lasers created new type of studies related to the laser processing of optically transparent materials (crystals, glasses, films, etc.) [5] for space-selective structure modification and fine tuning of its properties. This method known as a direct laser writing or femtosecond laser processing (FLP). FLP of glasses with particular chemical composition is known to make it possible to write, erase and rewrite various micro- [6, 7] and nanostructures [8] in the glass volume. At the same time, variation of laser parameters opens ways to

control the optical characteristics of the laser-written domains. In particular, the possibility of space-selective precipitation of Ag and CdS nanoparticles in the bulk of oxide glasses by femtosecond laser beam is promising for the fabrication of miniature optical components for nanophotonics, photovoltaics, optoelectronics, and data storage [9, 10].

Recently, one-step precipitation of silver nanoclusters and nanoparticles in phosphate glass under the femtosecond laser beam has been demonstrated [11]. The laser-induced domains have a yellow coloration and show tendency to photoluminescence and birefringence, the latter being dependent on the polarization of the writing laser beam. Similar studies on the formation of metal nanoparticles or semiconductor quantum dots were also carried out for silicate glasses [12, 13]. However, additional heat treatment of laser-modified glasses is generally required to precipitate and grow nanoparticles. It was shown [12] that only Ag⁺ ions are formed in a femtosecond laser-modified area. Additional heat treatment induces

aggregation processes which lead to an increase of photoluminescence intensity [13]. The similar behaviour is observed for laser processing of semiconductor-doped glass. Colourless and nonluminescent domains are formed after laser exposure of glasses but the following heat treatment of laser-written domains induces their photoluminescence due to the nanoparticle formation [14, 15]. The proposed technique allows precipitation of semiconductor nanoparticles in glass bulk, but its efficiency is poor due to the necessity of long-term heat treatment of laser-exposed glass.

Recently, our group has shown a possibility of direct laser-induced precipitation of CdS quantum dots in the bulk of silicate $K_2O-ZnO-B_2O_3-SiO_2$ glass [16]. In this regard, it is important to continue the investigation of the one-step precipitation of silver nanoclusters and nanoparticles under a femtosecond laser beam in the same glass host. Thus, this research is devoted to investigation and comparison of optical features of the domains laser-written in silicate and phosphate glasses doped with Ag and CdS.

2. EXPERIMENTAL

In this work, we synthesized silicate glass in the $K_2O-ZnO-B_2O_3-SiO_2$ system, concentration of silver was 0,1 wt.% (further marked as OS-0.1Ag) and that of CdS was 1 wt.% (OS-1CdS). Glass without dopants marked as OS was also synthesized. The batch was loaded into a corundum crucible at 1100°C. Glass melting was carried out in a laboratory electrical furnace at 1270°C for 1 h. To minimize volatilization of glass components, the crucible was covered with a fused silica cap. Resulting glass melt was poured into preheated to 500°C steel mould to prevent crackling of glass. Annealing of glass cast was performed in a muffle furnace at 500°C for 4 h with subsequent slow cooling to the room temperature. Also we investigated zinc phosphate glass in the $Ag_2O-ZnO-P_2O_5$ with 8 mol.% of Ag_2O marked as PZA-8, synthesized by the similar methodology.

Glass samples of 10x10x3 mm³ size were polished into plane-parallel plates for direct laser writing process. In our work, we used an experimental setup based on Pharos SP femtosecond laser system with 1030±2 nm central

wavelength which was tuned to 100 kHz pulse repetition rate and pulse duration of 180 fs. Pulse energy was varied in the range 100-400 nJ and each domain was written by a number of laser pulses varying from 10¹ to 10⁶. The laser beam was focused into the glass sample by an Olympus microscope objective (20X, N.A.=0.45) at the depth of ~150 µm under the surface. The glass sample was moved by means of a three-coordinate motorized air-bearing translation stage (Aerotech ABL1000) synchronized with the laser.

Optical characterization of the laser-written domains was performed using an Olympus BX41TF luminescence microscope equipped with a DP73 CCD camera. The photoluminescence excitation was provided by the mercury lamp and the Olympus U-MNV2 photoluminescence cube was used to separate emitted light from excitation one. Obtained optical and photoluminescence images of the written domains were analysed by means of ImageJ software. Study of cross-section slice of the domain written in PZA-8 glass sample was performed by transmission electron microscopy (TEM) using Titan 80-300 system (FEI, USA); the local elemental analysis was performed by energy-dispersive X-ray spectroscopy (EDS) combined with Titan 80-300 system.

3. RESULTS AND DISCUSSION

Set of ring-shaped domains was written in prepared glass samples by the focused femtosecond laser beam (Fig. 1). When a sample of OS-1CdS glass is exposed to 10⁶ laser pulses with energy over 300 nJ a strong yellow coloration is observed in the periphery of the domains, which may be caused by the precipitation of CdS nanoparticles in that area. At the same time, no coloration was observed for domains in OS-0.1Ag glass even at maximum values of pulse energy and number of pulses (Fig 1a). Increasing pulse energy from 100 to 400 nJ at 10⁶ pulses per dot resulted in an increase of the linear dimensions of the domains from 4.5 to 9.5 µm and from 4.5 to 12 µm for OS-0.1Ag glass and OS-1CdS glass, respectively. Thus, a variation of the pulse energy is an effective laser exposure parameter to control the size of the laser-written domains. Luminescence microscopy images (Fig. 1b) evidently show the

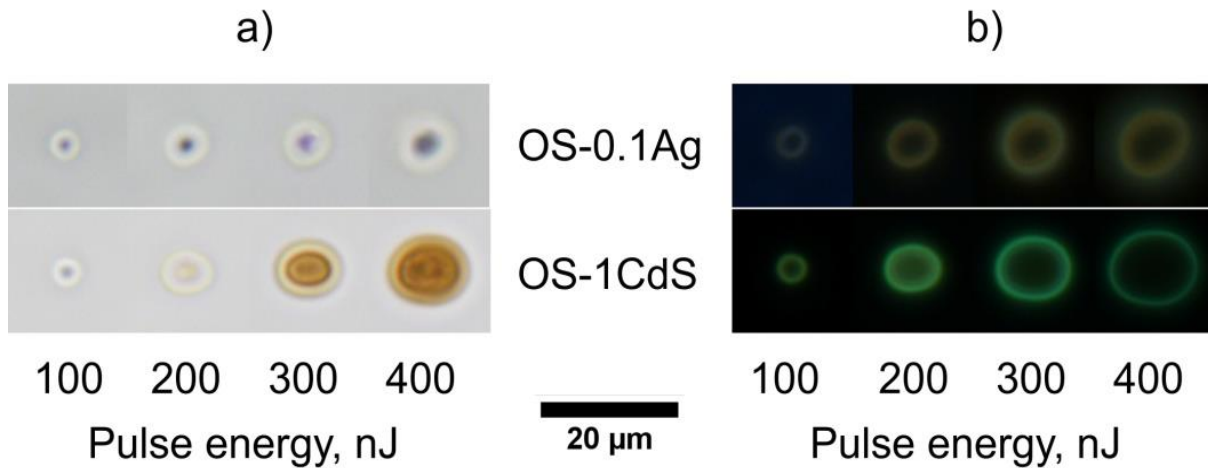


Figure 1. Optical (a) and photoluminescence (b) images of ring-shaped domains laser-written in OS-0.1Ag and OS-1CdS glass samples with different pulse energy from 100 to 400 nJ at 10^6 pulses. Luminescence excitation wavelengths – 400-410 nm, registration wavelengths – 455-800 nm.

photoluminescence occurrence on the periphery of the written domains. It should be mentioned that FLP of OS glass sample free of Ag or CdS also lead to the formation of ring-shaped domains while no coloration or photoluminescence was observed for this sample. It is also known that laser irradiation of glasses can induce the formation of radiation defects which caused yellowish to reddish coloration of glass and may be misinterpreted as nanoparticle precipitation [17]. These radiation

defects are thermally unstable and degrade after being heated up to 200-300°C. To confirm Ag or CdS precipitation and exclude a possible factor of radiation defects we performed a thermal treatment of both OS-0.1Ag and OS-1CdS laser-exposed glass samples at 350°C for 1 h. No degradation of photoluminescence from the laser-written domains was observed after the heat treatment.

A numerical analysis of photoluminescence intensity from the written domains showed that for

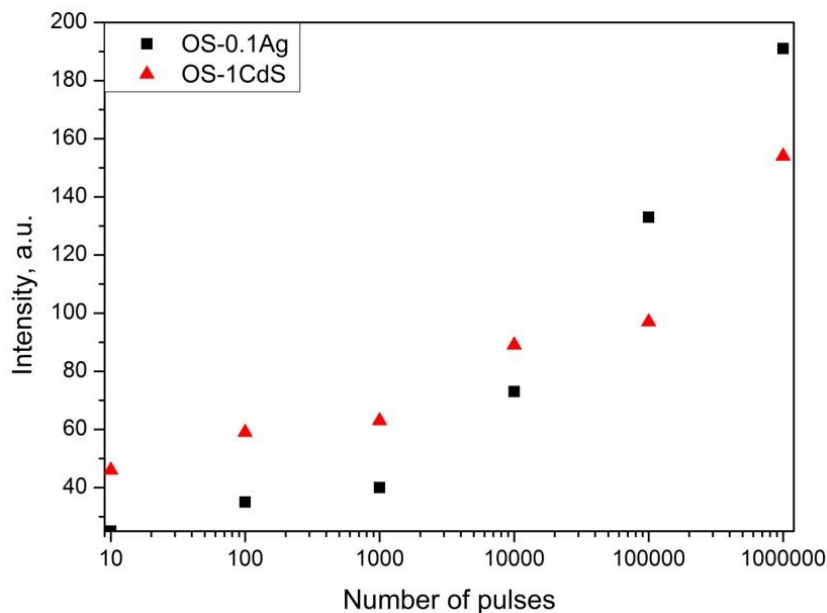


Figure 2. Luminescence intensity of written domains dependence on the number of laser pulses at 400 nJ pulse energy.

both studied glasses an increase in pulse energy up to 200 nJ leads to the formation of domains with maximum photoluminescence intensity. Importantly, the observed photoluminescence (Fig. 1b) lets us assert the formation of small nanoparticles of CdS and silver nanoclusters in the laser-written domains. The further increase in pulse energy resulted in photoluminescence quenching that can be related to the formation of large CdS particles in OS-1CdS glass and the beginning of the processes of aggregation of silver nanoclusters into larger agglomerates in OS-0.1Ag glass. It should be noted that simultaneous formation of both small and large nanoaggregates generally occurs in laser-written domain due to Gaussian energy distribution in the laser beam and corresponding temperature profile.

We also performed an analysis of photoluminescence intensity evolution with a number of writing laser pulses for domains written with 10^1 to 10^6 pulses at 400 nJ pulse energy (Fig. 2). One can see that the larger number of pulses, the higher photoluminescence intensity. The rate of the increase in the photoluminescence intensity is lower for OS-1CdS glass than for OS-0.1Ag glass

when number of pulses is 10^4 - 10^6 . This phenomenon can also be tentatively explained by the formation of large nanoparticles of CdS causing quenching of photoluminescence from smaller particles.

When comparing the results obtained for glasses OS-0.1Ag and OS-1CdS, it is important to take into account the concentration of the dopant. In this work, the concentration of silver in glass OS-0.1Ag was 10 times lower than the concentration of CdS in glass OS-1CdS, but when comparing the photoluminescence intensities of the written domains, we obtained relatively similar results. Thus the determination of the optimal concentration of particular dopant in glass is required for achieving the maximum photoluminescence intensity of the written domains. This determination will be done by studying silicate glasses with different concentrations of photosensitive dopants. Also by varying the parameters of FLP (pulse energy and number of pulses) it is possible to record data in the photoluminescence intensity signal of written domains in several levels of intensity which is open

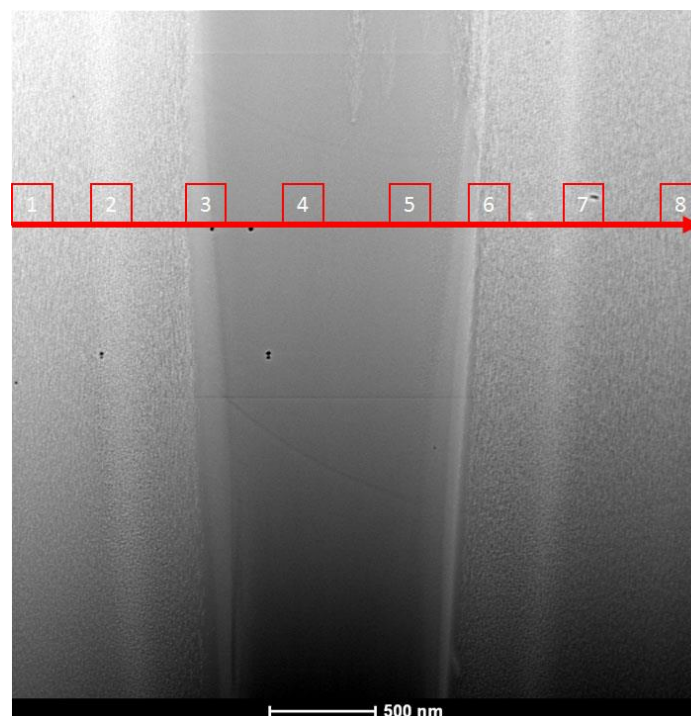


Figure 3. TEM image of cross-cut from the domain laser written in PZA-8 glass sample. Direction of laser beam: up-down. Red arrow shows direction of EDS scan; numbers refer to EDS measurements on Fig. 4.

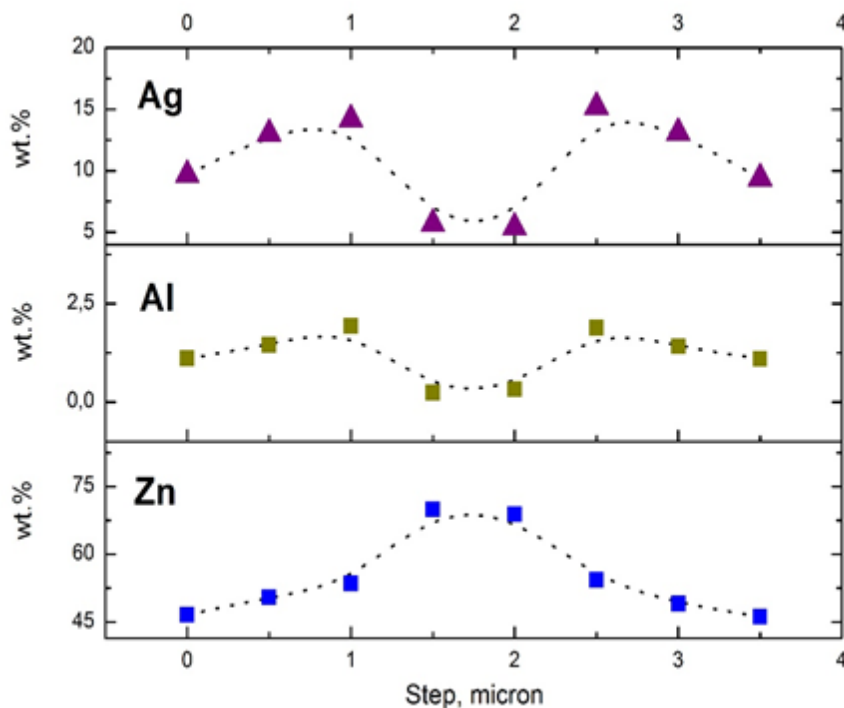


Figure 4. Results of local EDS measurements of cross-section from Fig.3.

routes for multilevel data recording in the bulk of robust and chemically stable silicate glass.

In recent works [11, 18, 19] we studied formation of silver particles (both clusters and plasmonic nanoparticles) in zinc phosphate glasses referred as PZA. We showed that by tuning FLP parameters it is possible to locally precipitate Ag nanoparticles in glass. In this work by means of TEM and EDS we studied phenomenon of local ions migration during FLP.

Fig.3 shows TEM image of cross-cut obtained by ion beam etching of domain laser written in PZA-8 glass sample at 100 nJ and 10^6 laser pulses. Since glass network formers have a stronger binding energy with oxygen than the network modifiers, they tend to remain at the center of the domain's area. Thus FLP of glasses doped with noble metal ions (Au, Ag) that always act as network modifiers, leads to the precipitation of metal nanoparticles and formation of structures with unique optical properties such as surface plasmon resonance or photoluminescence. In all previous studies concerning silver or gold doped glasses, thermal treatment near the glass transition temperature was reported to induce homogeneous

volume precipitation of metal nanoparticles inside the glass [20-23]. Generally, this originates from the reducing of Ag/Au ions to neutral atoms with the help of reducing agents (SnO_2). Neutral metal atoms tend to agglomerate within the formation of metal nanoparticles. In our case we performed one-step precipitation of silver clusters and nanoparticles that is confirmed by TEM revealing chemical contrast in central and side areas of cross-cut. This difference gives preliminary insights in the spatially-selective ion migration process occurred during the FLP of glass.

In order to confirm ion migration in phosphate glass we performed EDS measurements in eight points along cross-section according to Fig.3. Fig. 4 shows results of EDS measurements. One can see that silver concentration is slightly higher in periphery areas and lower in central area. Same effect can be seen for aluminium ions which were introduced in glass during melting in corundum crucible. On the other hand, zinc concentration increased is central area that is typical for network former components.

Comparing results for FLP of silicate and phosphate glasses one can see significant

similarities that are expressed in local changes of chemical composition and element redistribution. Both type of glasses poses photoluminescence on the edges of laser written domains due to precipitation of Ag clusters or CdS quantum dots. At once structural peculiarities of phosphate network allow to obtain glasses with much larger content of silver comparing to silicate glass.

4. CONCLUSIONS

We showed that FLP is a useful technique for one-step spatially-selective formation of micron-sized photoluminescent domains in the bulk of Ag- and CdS-doped glasses by the example of silicate and phosphate glasses. It was demonstrated that the precipitation and growth of photoluminescent Ag nanoclusters and CdS quantum dots occur in the periphery of laser-written domains. We managed to control the size and optical characteristics of laser-written domains by varying pulse energy and number of pulses. Also, we confirmed occurrence of ion migration process in silver doped zinc phosphate glass. FLP of glass leads to migration of glass network modifiers (such silver) to the periphery of written domains, while migrations of network formers direct to the central area of domains. Obtained results give important information about possibilities of local chemical change and open a prospect of FLP for application in multilevel optical data storage and optical waveguides.

ACKNOWLEDGMENTS

This study was financially supported by the Russian Foundation for Basic Research (grant 18-33-00595 and 19-32-80032).

REFERENCES

- [1] A.I. Ekimov and A.A. Onushchenko, *JETP Lett.* **34(6)**, 345 (1981).
- [2] D. Ricard, P. Roussignol, and C. Flytzanis, *Opt. Lett.* **10**, 511 (1985).
- [3] I. Belharouak et al. *J. Non-Cryst. Solids* **244**, 238 (1999).
- [4] N.F. Borrelli et al. *J. Appl. Phys.* **61**, 5399 (1987).
- [5] Rafael R. Gattass, and Eric Mazur, *Nature photonics* **2(4)**, 219 (2008).
- [6] A.S. Lipatiev et al., *Cryst. Growth Des.* **17(9)**, 4670 (2017).
- [7] A.S. Lipatiev et al., *CrystEngComm* **20(22)**, 3011 (2018).
- [8] J.M.P. Almeida et al., *Opt. Express* **20(14)**, 15106 (2012).
- [9] D.Tan, K.N. Sharafudeen, Y. Yue, and J. Qiu, *Prog. Mater. Sci.* **76**, 154 (2016).
- [10] G.Bell, et al. *Applied Physics Letters* **108(6)**, 063112 (2016).
- [11] G.Yu. Shakhgildyan et al., *J. Non-Cryst. Solids* **481**, 631 (2018).
- [12] Y. Miyamoto et al., *Radiat. Meas.* **46**, 1480 (2011).
- [13] Y. Dai et al., *Chem. Phys. Lett.* **439**, 81 (2007).
- [14] P. Mardilovich et al. *Optical Materials* **34(11)**, 1767-1770 (2012).
- [15] P. Mardilovich et al., *Applied Physics Letters* **102(15)**, 151112-5 (2013).
- [16] M.P. Vetchinnikov et al., *Opt. Lett.* **43**, 2519 (2018).
- [17] V.N. Sigaev et al., *Nanotechnology* **24(22)**, 225302 (2013).
- [18] A.S. Lipatiev et al., *Glass and Ceramics* **73(7-8)**, 277-282 (2016).
- [19] G.Yu. Shakhgildyan et al., *Glass and Ceramics* **73(11)**, 420-422 (2017).
- [20] J. Qiu et al., *Applied Physics Letters* **81(16)**, 3040-3042 (2002).
- [21] H. Zeng et al., *Journal of Physics: Condensed Matter* **16**, 2901-2906 (2004).
- [22] Y. Dai et al., *Chemical Physics Letters* **439**, 81-84 (2007).
- [23] J. Qiu et al., *Optics Letters* **29(4)**, 370-372 (2004).

Piezoelectric and ferroelectric properties of various amino acids and tubular dipeptide nanostructures: Molecular modelling

V. S. Bystrov^{1,*}, I. K. Bdikin² and Budhendra Singh^{2,3}

¹*Institute of Mathematical Problems of Biology, Keldysh Institute of Applied Mathematics, RAS, 142290 Pushchino, Moscow region, Russia*

**Corresponding author, e-mail address: vsbys@mail.ru*

²*TEMA-NRD, Mechanical Engineering Department and Aveiro Institute of Nanotechnology (AIN), University of Aveiro, 3810-193 Aveiro, Portugal*

³*Department of Physics, Central University of South Bihar, Gaya-Panchanpur Road, Gaya-824236, India*

Received 19 November 2019; accepted 20 February 2020; published online 10 March 2020

ABSTRACT

Piezoelectric and ferroelectric properties of dipeptide nanotubes (PNT) based on phenylalanine (F), alanine (A) and branched-chain amino acids (BCAAs) isoleucine (I), leucine (L) are investigated. Homodipeptides, such as di-isoleucine (II), di-leucine (LL), and heterodipeptides alanine-isoleucine (AI) dipeptides, and di-phenylalanine (FF), are studied by molecular modeling using a quantum-mechanical (QM) semi-empirical PM3 method in a restricted Hartree-Fock (RHF) approximation based on the HyperChem package. After optimization of the models by the Polak-Ribiere conjugate gradient method, the total dipole moment and polarization of PNTs are calculated, with orientation along c-axis of a PNT with L-chiral isomer and alpha-helix conformation. The values obtained are: Pz (LL) ~ 3.6 $\mu\text{C}/\text{cm}^2$, Pz (II) ~ 6 $\mu\text{C}/\text{cm}^2$, Pz(AI) ~ 8.02 $\mu\text{C}/\text{cm}^2$, Pz(FF) ~ 2.3 $\mu\text{C}/\text{cm}^2$, which are comparable with the known data on the phenylalanine (FF) PNT polarization (for L-chiral in beta-conformation), which are of the order of Pz ~ 4 $\mu\text{C}/\text{cm}^2$. These polarizations allow us to calculate the piezoelectric coefficients d_{33} along the c-axis (in accordance with known electromechanical coupling relationship): 1) $d_{33}(\text{LL}) \sim 8 \text{ pm/V}$, $d_{33}(\text{II}) \sim 10 \text{ pm/V}$, $d_{33}(\text{AI}) \sim 26 \text{ pm/V}$, $d_{33}(\text{FF}) \sim 35 \text{ pm/V}$ (for $\epsilon = 4$); 2) $d_{33}(\text{LL}) \sim 12 \text{ pm/V}$, $d_{33}(\text{II}) \sim 15 \text{ pm/V}$, $d_{33}(\text{AI}) \sim 39 \text{ pm/V}$, $d_{33}(\text{FF}) \sim 52 \text{ pm/V}$ (for $\epsilon = 6$). These results are comparable with earlier data for FF PNT $d_{33}(\text{FF}) \sim 50 \text{ pm/V}$ (in beta-sheet conformation, L-chirality). The data obtained are confirmed by corresponding experimental AFM/PFM observations and measurements.

1. INTRODUCTION

All amino acids (AA) have their own dipole moments [1, 2], which interact with one another while amino acids or their dipeptides and polypeptides self-assemble into more complex molecular structures [3], such as molecular crystal structures (for example, based on the AA Glycine in various polymorphic forms [4-6]), various tubular structures, such as dipeptide nanotube (PNT) [7-12] and ion channel structures in biological

membranes [13 - 17]. Many of them are useful in materials science and medicine. It is established that many of these structures possess piezoelectric and ferroelectric properties [9-12, 18, 19]. Many similar organic structures having ferroelectric properties are considered now as organic ferroelectrics [19, 20]. Such structures based on AA, as well as on various DNA bases or other biological structures, demonstrating ferroelectricity (and piezoelectricity) are called bioferroelectrics (and biopiezoelectrics). They were intensively

studied by different methods, both experimentally and theoretically [6, 9-14]. As is well known, piezoelectricity usually arises as a result of electromechanical coupling in a given material [2, 12, 13]. This coupling is well known in biology – it can be observed in many biological processes: in a voltage-controlled muscle movement, in the nervous system, and in ion transport. [1, 13]. So this electromechanical coupling can be considered as the heart of ferroelectric and bioferroelectric phenomena.

A useful approach for such studies is computer molecular modeling, which allows one to calculate, investigate and predict the main physical properties of these structures based on AA. For example, diphenylalanine (FF) PNTs have been recently considered theoretically using molecular modeling by the quantum-chemical PM3 method (in HyperChem software) and experimentally using atomic force microscopy (AFM)/piezo-response force microscopy (PFM) measurements [9-12, 21-23].

But not only PNTs having aromatic (benzene) rings, such as FF, can demonstrate piezo/ferroelectric properties.

As pointed out by Leuchtag [13, 16], the branched-chain amino acids (BCAAs) Isoleucine (I), Leucine (L) and Valine (V), are known to exhibit ferroelectric properties with extremely large values of spontaneous polarization and dielectric permittivity [24, 25]. In the present work the piezoelectric and ferroelectric properties of the PNTs based on BCAA homodipeptides such as di-isoleucine (II), di-leucine (LL) and the heterodipeptide alanine-isoleucine (AI) are studied using molecular modeling by the PM3 method, and using experimental AFM/PFM measurements.

Here we deal only with α -helix conformations and L-chiral initial BCAAs molecules. D-chiral (the same as in a recent study [26]) and beta-sheet conformations (which were earlier used for FF PNT [9-12, 21-23]) will be considered later. It is known from experimental X-ray measurements that FF PNTs have the shape of an isolated ring with six dipeptides that form parallel stacking of two rings to form a crystal hexagonal structure [8] or two-layer rings in tubular models of these PNTs [11, 23]. However, for PNTs with BCAAs, only four dipeptides can form a similar isolated ring and construct a crystal structure [8, 27], as well as

similar tubular models of PNT[11, 23].

In this work we consider the structures and properties of several amino acids, their dipeptides and corresponding tubular nanostructures by molecular modeling using HyperChem package within the quantum-chemical semi-empirical PM3 approach in restricted Hartree-Fock (RHF) and unrestricted Hartree-Fock (UHF) approximations. The main results of computational data obtained for polarization and piezoelectric properties (piezoelectric coefficients d_{33}) are analysed in comparison with other known data and experimental observations.

2. COMPUTATIONAL DETAILS AND MAIN MODELS

In this work, the main tool used for the molecular modelling of all the studied nanostructures was the HyperChem 8.01 package [28]. Various computational methods were used, such as the molecular mechanics (MM) methods (including MM+, Amber, BIO CHARM), quantum mechanical (QM) self-consistent field (SCF) Hartree-Fock (HF) calculations, and semi-empirical methods (such as PM3, ZINDO-1), in the restricted Hartree-Fock (RHF) and unrestricted Hartree-Fock (UHF) approximations. The use of both the MM and QM methods for molecular modeling allowed us to obtain the minimum of the total energy or the potential energy surface (PES) of the systems being modelled. As a result, all the molecular systems investigated reached their optimal atomic configuration. The optimization of molecular systems and finding of their optimal geometry is performed in this work using the Polak–Ribere (conjugate gradient method) algorithm, which determines an optimized geometry at their minimum total energy point (using PES). These computational methods were used for detailed debugging, validation and testing of the models. But for final calculations of the optimized models, the PM3 in RHF approximations were used (since both UHF and RHF approximations show the same results for the studied systems).

3. MAIN RESULTS AND DISCUSSIONS

First we investigate the initial amino acid properties. In HyperChem tool there is a special database for the main amino acids and we take it

for our modeling in HyperChem workspace. One of the important features is that all the amino acids (as well as dipeptides and polypeptides) exist in the initial pristine forms, but in all solutions (usually containing water) and in all reactions in living organism they exist in zwitterionic form. These forms can be created in HyperChem workspace

using a special option and we can work further with these zwitterionic structures. Another important feature is that all AA can exist in various conformations and chiralities (isomers). In this work we use alpha-helix conformation and L (left, from the Latin “laeva”) chirality.

Table 1. Several Amino Acid (AA) characteristics. (All atom colours are shown in the Fig.1 caption)

#	Amino Acid	Structure		I / ZW	D, Dipole moment, Debye	Polarization, C/m ²	Type
		I (initial pristine)	ZW (zwitterionic)				
1	Glycine (Gly, G)			I ZW	1.8 11.5	0.1 0.6	SC
2	Alanine (Ala, A)			I ZW	1.85 11.03	0.087 0.45	HSC
3	Phenylalanine (Phe, F)			I ZW	2.938 10.56	0.0676 0.2276	BSC
4	Leucine (Leu, L)			I ZW	2.763 10.013	0.0766 0.2562	BCAA
5	Iso-leucine (Ile, I)			I ZW	2.814 9.926	0.078 0.2538	BCAA
6	Valine (Val, V)			I ZW	1.396 9.973	0.045 0.292	BCAA

3.1. Dipole moments and polarizations of various amino acids

The possibility of a piezoelectric effect in various amino acids was indicated earlier by Lemanov [29, 30]. It should be noted that many of the amino acids considered by us have non-centrosymmetrical elements. This suggests a possibility of a piezoelectric effect in them. So, for example, valine, leucine, isoleucine have a symmetry group $P2_1$, and alanine and phenylalanine – $P2_12_12_1$ (while diphenylalanine exhibits hexagonal symmetry $P6_1$ [8]). In addition, like crystals based on glycine and diphenylalanine structures, these AAs have high polarizability, which is manifested when exposed to an electric field. This can be investigated using simulation methods which were described in [9-12, 31, 32].

Firstly we consider, the values of the dipole moment and polarization. Using the HyperChem tool and the database of amino acids we calculate

these values using RHF PM3 approach. As a result, we obtained data Table 1.

Abbreviations of AA Type in Table 1 are: Glycine – is a simplest special case (SC); all the other AA are the AA with Hydrophobic side chain (HSC): Alanine is the simplest of them; Phenylalanine is AA with an aromatic benzyl side chain (BSC); Leucine, Isoleucine and Valine are the branched-chain AA (BCAA).

As Table 1 shows, upon transition to the zwitterionic form, the dipole moment D increases significantly, which is not surprising, since in this ZW form the polar groups NH_3^+ and COO^- are more pronounced and are located at large distances from each other. The polarization value is:

$$P = 3.33556255 \cdot D/V \text{ (in C/m}^2\text{)},$$

where V is the structure's volume within the Van der Waals surface.

3.2. Di-peptides and Nanotubes of various AA

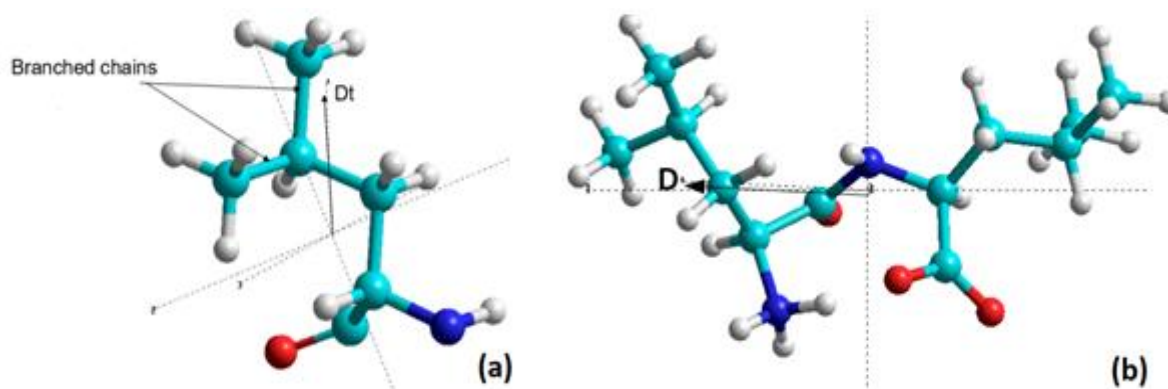


Figure 1. Structures based on the Leucine AA in ZW from: a) one molecule Leu, b) dipeptide Leu-Leu (LL). Atomic colour: Red – Oxygen, Deep Blue – Nitrogen, Cyan – Carbon, Gray – Hydrogen. The same for all atoms below too.

Table 2. Data calculated for Leucine AA structures.

Structure	Dipole, Debye	Polarization P, C/m ²	Dipole in ZW opt, Debye	Polarization P C/m ²	Dipole PNT Dt = ~ Dz, Debye	Volume of PNT, Å ³	Polarization P~Pz of PNT, C/m ²
Leu 1	2.763	0.077	10.013	0.2562			
di-leu			10.6194	0.14556			
4-di-leu in 1 ring					8.21	965.01	0.02838
2 rings di-leu					20.555	1928.27	0.03556

Next, we consider dipeptides primarily based on AA with the branched side chains (BCAA): namely, Leucine-Leucine (LL), Isoleucine-Isoleucine (II) and heterodipeptide, alanine-Isoleucine (AI).

3.2.1. Leucine (Leu or L) Leu-Leu or LL dipeptide

As we can see from the previous section (Table 1) - Leucine (Leu, or L) has its own initial dipole moment $D \approx -2.7$ Debye, in ZW form it is equal to $D \sim 10$ Debye.

Using the HyperChem tool we constructed a dipeptide in ZW form and calculated its properties

for a fixed atomic position (single point – SP – calculation). Then we performed PES optimization using the Polak–Ribere conjugate gradient method and obtained an optimized structure. The data obtained are presented in Fig. 1 and in Table 2 below.

After that we constructed 1 ring from 4 di-leucine (4-LL) and optimized it in a similar way. Finally, we designed a 2-ring peptide nanotube (PNT) model and optimized this structure. The results are presented in Fig 2,3 and the data computed are listed in Table 1, 2. Having compared the results obtained with experimental data [8] we can see that the shape of PNT is fully consistent

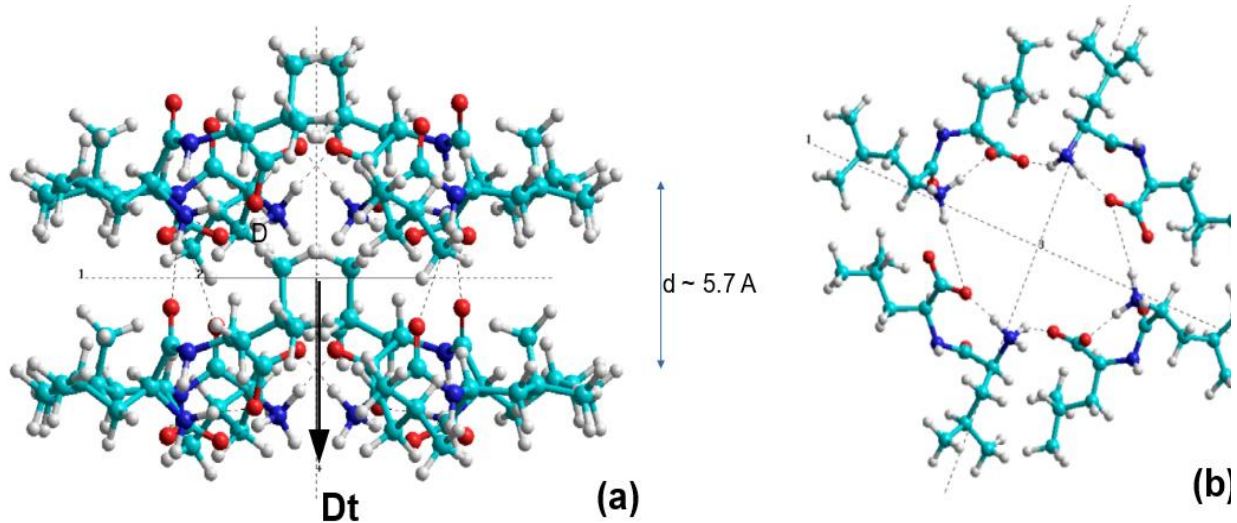


Figure 2. Tubular LL structures: a) side view (Y axis), b) top view (Z axis).

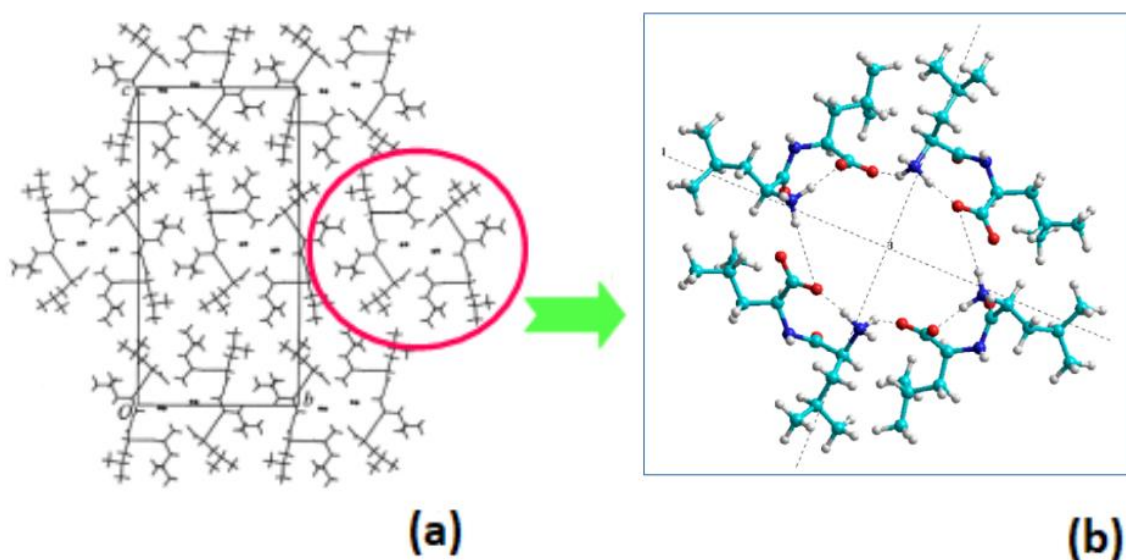


Figure 3. Comparison of LL PNT structure with experimental data from Gorbitz [8].

with the data obtained by X-ray. The experimental data for LL crystal orthorhombic unit cell are the following: $a = 5.3524 \text{ \AA}$, $b = 16.7600 \text{ \AA}$, $c = 33.312 \text{ \AA}$ (space group P212121). For our model, we have $a \sim 5.7 \text{ \AA}$ and the inner hollow width is approximately $\sim 8 \text{ \AA}$, which corresponds to doubled parameter b

$\sim 16 \text{ \AA}$.

3.2.2. Isoleucine (Ile or I) Ile-Ile or II dipeptide

For Isoleucine, the data obtained by similar calculations are presented below in Fig. 4,5 and Table 3.

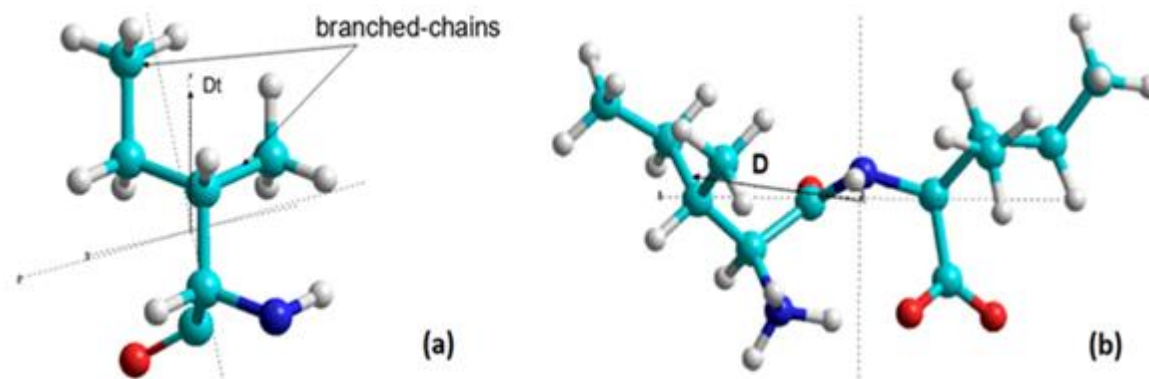


Figure 4. Structures based on Isoleucine AA in ZW form: a) one molecule Ile, b) dipeptide Ile-Ile (II)

Table 3. Data calculated for Isoleucine AA structures.

Structure	Dipole D, Debye	Polarization P, C/m ²	Dipole in ZW form, Debye	Polarization P in ZW, C/m ²	Dipole PNT Dt = ~ Dz, Debye	Volume of PNT, Å ³	Polarization P~Pz of PNT, C/m ²
Ile 1	2.814	0.078	9.926	0.2538			
di-Ile			11.7321	0.16064			
4-di-Ile 1 ring					16.7232	962.96	0.06017
2 rings di-Ile					35.180	1918.73	0.06116

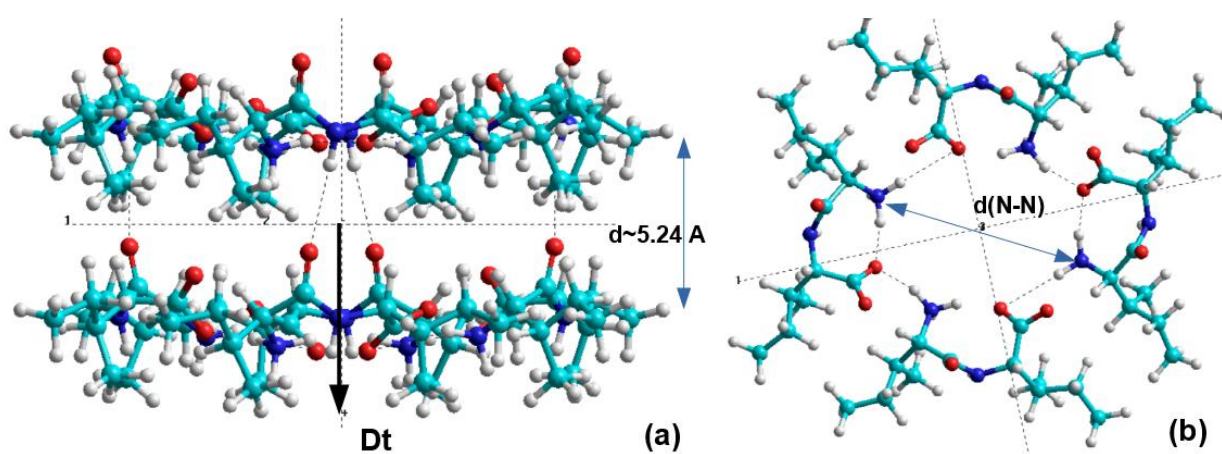


Figure 5. Tubular II structures: a) side view (Y axis), b) top view (Z axis); $d(\text{N-N}) \sim 8.0 - 8.5 \text{ \AA}$.

3.2.3. Alanine-Isoleucine (Ala-Ile) and AI dipeptide

For Alanine-Isoleucine combined structures similar calculations data obtained are presented below in Fig. 6, 7 and Table 4.

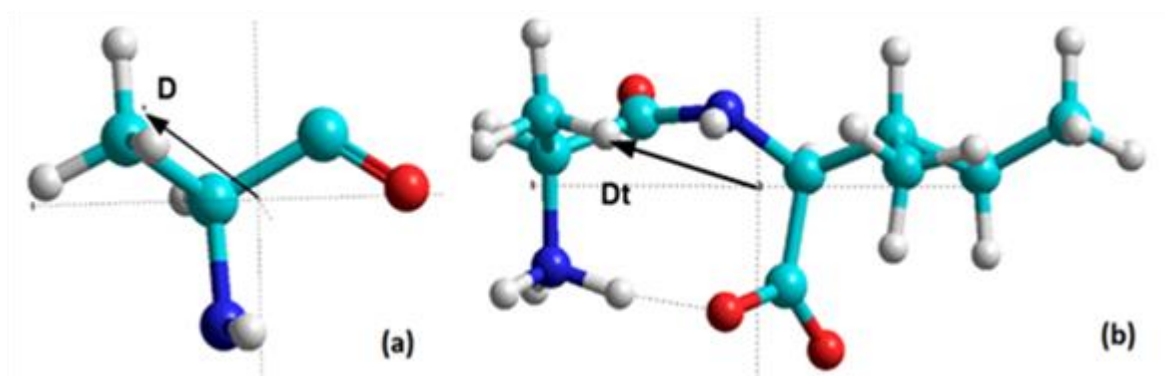


Figure 6. Structures based on the Alanine-Isoleucine AI in ZW form: a) one molecule Ala, b) dipeptide AI

Table 4. Data calculated for Alanine-Isoleucine AI structures.

Structure	Dipole D, Debye	Polarization P, C/m ²	Dipole in ZW form, Debye	Polarization P in ZW, C/m ²	Dipole PNT Dt = ~ Dz, Debye	Volume of PNT, Å ³	Polarization P~Pz of PNT, C/m ²
Ala 1	2.375	0.1113					
Ala-Ile			10.358	0.1782			
4-Ala-Ile 1 ring					15.0338	771.19	0.06502
2 rings Ala-Ile					36.869	1533.39	0.08020

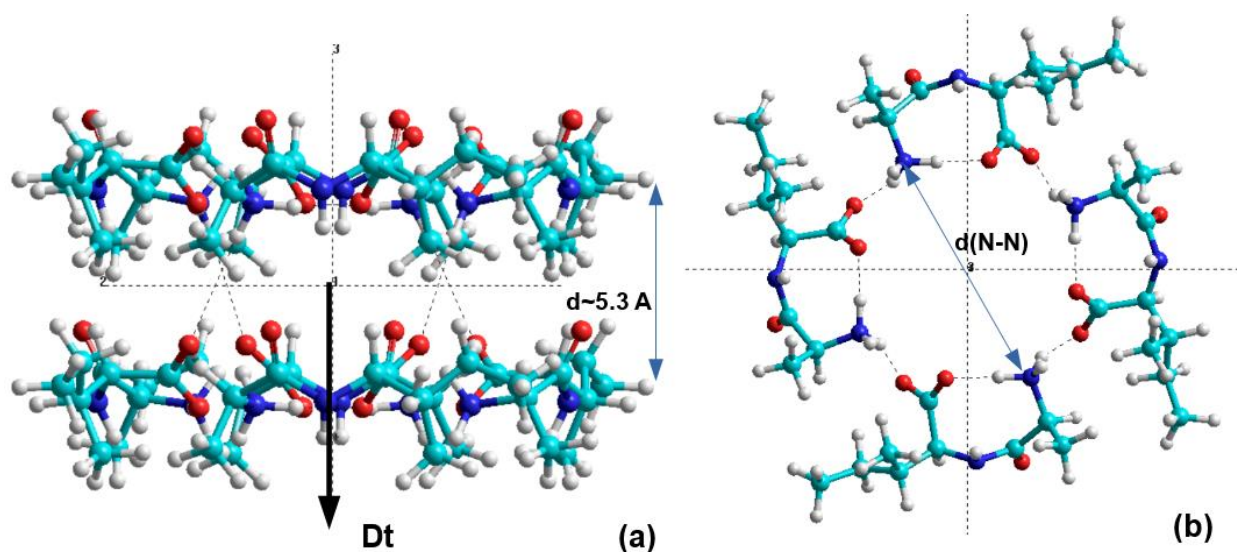


Figure 7. Tubular AI structures: a) side view (Y axis), b) top view (Z axis); average $d(N-N) \sim 8.1 \text{ \AA}$.

3.3. Piezoelectric coefficients calculations

In works [8, 27] the structures of AA crystals were studied, but the piezoelectric properties were not calculated. Now we can calculate the piezoelectric properties based on the common coupling of the local deformation of any materials in the electric field [2, 9-12].

Piezoelectricity is a phenomenon that can exist only in non-centrosymmetrical materials [2, 9]. The main building blocks of life are proteins, and the majority of protein crystals are non-centrosymmetrical. Proteins are made of combinations of 21 known amino acids [1], the majority of which also have the form of non-centrosymmetrical crystal structures. In the works by Lemanov *et al.* [29, 30] it was demonstrated that, as a consequence, these amino acids possess piezoelectric properties. He revealed the piezoelectric response of amino acid crystals, and attributed it to the rotation of the CH₃ and NH₃ groups [29, 30]. A similar common piezoelectric response is inherent in almost all organic and biological structures. Such biopiezoelectricity is exhibited in large-scale biological systems such as proteins, biopolymers, polysaccharides, organelles, and various organic piezoelectric biomaterials [9-20, 33-35].

As was already mentioned above, piezoelectricity arises from the electromechanical coupling in any given material [2, 9-12]. We can assume that biopiezoelectricity also arises from electromechanical coupling in bioorganic molecular nanostructures. The phenomenon is based on the known general relation between the piezoelectric constant d_{ik} , the electrostriction coefficient Q_{ik} , the permittivity of the material ϵ , the permittivity of vacuum $\epsilon_0 = 8.85 \cdot 10^{-12} \text{C}/(\text{Vm})$, and the component of polarization P_k of the whole system [2, 11, 36]. For a simple case, as a first approximation for only one component of the coefficient Q_{11} , the piezoelectric constant d_{33} , dielectric permittivity ϵ and spontaneous polarization P , the relationship can be written as [36, 37]:

$$d_{33} = 2Q_{11}\epsilon\epsilon_0P \quad (1)$$

On this basis, we can study piezoelectricity and

related changes in the dipole moments and polarization of various systems. We should only remember, that with such a local deformation of the material (or any molecular structure) under the influence of an electric field, in eq. (1), it is precisely the corresponding change in polarization, that must be taken into account. Therefore, the polarization P must be replaced by ΔP .

For example, using our data on the polarization of the computed AA (from Table 2, 3 and 4: $P(\text{LL}) \sim 0.036 \text{ C}/\text{m}^2$, $P(\text{II}) \sim 0.06 \text{ C}/\text{m}^2$, $P(\text{AI}) \sim 0.08 \text{ C}/\text{m}^2$) and the data obtained from the calculations for a similar structure FF PNT in our previous work [9-12] ($Q_{11} \sim 350 \text{ m}^4/\text{C}^2$, $\Delta P \sim 0.05P$ for the case of applied external electrical field along the main axis of PNT $E_z \sim 0.001 \text{ a.u.} \sim 5.14 \cdot 10^8 \text{ V}/\text{m}$), the values of piezoelectric coefficients for our tubular models of the investigated AA PNT (with $\epsilon = 4$ as in proteins) were estimated: $d_{33}(\text{LL}) \sim 44 \text{ pm}/\text{V}$, $d_{33}(\text{II}) \sim 73 \text{ pm}/\text{V}$, $d_{33}(\text{AI}) \sim 99 \text{ pm}/\text{V}$ [38]. These data are in good agreement with earlier obtained $d_{33}(\text{FF}) \sim 50 \text{ pm}/\text{V}$ for FF PNT [9-12].

However, we must take into account that such an estimate is very approximate and perhaps it gives overestimated values. Therefore, below we will conduct a more accurate and consistent calculation of such a local deformation of each of the studied tubular structures in the same electric field $E_z \sim 0.001 \text{ a.u.} \sim 5.14 \cdot 10^8 \text{ V}/\text{m}$, applied along the main OZ- axis of each AA PNT structure.

As usual, the value of the polarization P is obtained from the dipole moment D (in Debye units):

$$P = 3.33556255 \cdot D/V \quad (\text{in } \text{C}/\text{m}^2),$$

where V is the structure's volume on the Van der Waals surface.

3.3.1. Procedure of calculations

The molecular models of all the studied PNT were constructed using the database of amino acids (AA) from HyperChem tool [28]. All AA and relevant di-peptides were taken out in alpha helix conformation and in L chirality. (an exception was only for diphenylalanine, which was used besides alpha-helix, also in beta-sheet conformation for comparison with previous data [11, 12, 23, 26]).

First, after construction of the molecular models of any AA PNT, their structural optimization (by

Polak–Ribere conjugate gradient method) was performed to reach the most optimal nanostructure of AA PNT. All necessary parameters of these optimized AA PNT structures (such as dipole moment, volume, polarization, etc.) were calculated at this stage. These data are listed above in Table 2, 3 and 4.

Second, the electric field E_z along the main tubular axis of AA PNT was applied (using a special option in the HyperChem tool) and for the

optimized structure (with fixed positions of all the atoms) Single Point (SP) calculations were performed to obtain the changes of the dipole moment $\Delta D = D - D_0$ and polarization $\Delta P = P - P_0$ in this case. From these data, the value of electronic polarizability α for each PNT structure was estimated, relying on the fact that the deviation of the electric field ΔE_z is reckoned from $E=0$, $\Delta E_z = E_z$. These data of the polarizability $\alpha = \Delta D/E_z$ could be converted to atomic units (from

Table 5. Computed data for various AA PNT characteristics and parameters. (all the structures are in alpha-helix conformation and L-chirality, except for the last column with old L-FF data in beta-sheet conformation).

Parameter	L-Leu-Leu	L-Ile-Ile	L-Ala-Ile	L-FF-alpha [23, 26]	L-FF-beta [23]	L-FF-beta, old data [11,12]
$D_0=D_z$, Debye	20.56	35.18	36.87	23.89	38.29	42.70
$P_0=P_z$, C/m ²	0.036	0.061	0.080	0.023	0.037	0.041
$D(E_z=0.001 \text{ a.u.})$, fixed SP	18.37	32.98	35.09	19.54	33.19	37.45
$\Delta D=D-D_0$, Debye (in abs. value)	1.98	2.20	1.78	4.35	5.10	5.26
$\alpha=\Delta D/\Delta E$, Å ³	115.62	128.04	104.02	253.62	297.58	306
$\alpha=\Delta D/\Delta E$, a.u.	780.22	864.03	701.93	1711.54	2008.2	2068
D^{OPT} (opt. in $E_z=0.001 \text{ a.u.}$)	17.208	31.773	32.904	17.183	32.004	35.73
ΔD^{OPT} (opt. in E_z)	1.165	3.407	2.181	2.355	1.187	1.712
ΔP^{OPT} (opt. in E_z), C/m ²	0.002	0.006	0.005	0.002	0.001	0.002
$(\Delta P^{\text{OPT}})^2$, C ² /m ⁴	$4.06 \cdot 10^{-6}$	$3.513 \cdot 10^{-5}$	$2.25 \cdot 10^{-5}$	$5.102 \cdot 10^{-6}$	$1.3059 \cdot 10^{-6}$	$3.888 \cdot 10^{-6}$
V_0 , Å ³	1928.27	1918.73	1533.39	3477.59	3464.29	3503.17
$V(\text{opt})$, Å ³	1928.70	1917.27	1530.42	3481.49	3463.21	3498.42
$\Delta V=V-V_0$, Å ³	0.43	1.460	2.97	3.90	1.09	4.75
$S= \Delta V/V_0$	$2.23 \cdot 10^{-4}$	$7.62 \cdot 10^{-4}$	0.00194	0.00112	$3.1768 \cdot 10^{-4}$	0.0017
$Q=S/(\Delta P^{\text{OPT}})^2$, m ⁴ /C ²	54.95	21.68	77.26	219.64	243.20	348.80
$d=2\epsilon\epsilon_0 Q \Delta P^{\text{OPT}}$, ($\epsilon = 4$), pm/V	8.0	10.0	26.0	35.0	20.0	48.7~50.0
$d=2\epsilon\epsilon_0 Q \Delta P^{\text{OPT}}$, ($\epsilon = 6$), pm/V	12.0	15.0	39.0	52.5	30.0	73.0
$d=2\epsilon\epsilon_0 Q \Delta P^{\text{OPT}}$, ($\epsilon = 10$), pm/V	20.0	25.0	65.0	87.5	50.0	121.8

Debye unit for D) using the coefficient 1 Debye = 0.393456 a.u., with $E_z = 0.001$ a.u. The presentation of α in angstrom (\AA) unit can be made by dividing into the coefficient 6.74833: $\alpha(\text{\AA}^3) = \alpha(\text{a.u.})/6.74833$.

Thrid, the structural optimization (using again Polak–Ribere conjugate gradient method) under applied electric field E_z was carried out to reach a new optimal structure under the influence of this applied electric field. After this optimization all the atoms of PNT structures changed their positions and the total volume of the structures was changed to $-\Delta V = V - V_0$. For these new optimized PNT structures, all necessary calculations were performed again to obtain new changed data for dipole moments D^{OPT} (and $\Delta D^{\text{OPT}} = D^{\text{OPT}} - D$ in E_z), volume V and polarization P^{OPT} (and $\Delta P^{\text{OPT}} = P^{\text{OPT}} - P$ in E_z). As a result, the electrostriction and piezoelectric coefficients were calculated from these data obtained.

Electrostriction coefficient is determined by relation $Q_{11} = Q = S/(\Delta P^{\text{OPT}})^2$, where $S = \Delta V/V_0$.

Piezoelectric coefficient is finally calculated from the relation $d_{33} = d = 2\epsilon\epsilon_0 Q \Delta P^{\text{OPT}}$.

All the data, computed step by step using this procedure algorithm, are presented in Table 5.

Table 5 lists the data not only for AA PNT (LL PNT, II PNT and AI PNT) computed in this work, but also the data obtained from our previous works on FF PNT (last columns). The last data are also compared with our older calculations of FF PNT in beta-sheet conformation. As one can see, these data are slightly overestimated as compared to our earlier results due to a greater value of the volume deformation and electrostriction coefficient calculation. As a result, the value of the piezoelectric coefficient has a greater value too as compared to our present result. The reason is probably that due to some details of optimization of the models, which improved the initial structures, we followed a different PES optimization trajectory and got to a different PES minimum point.

In Table 5 several various values of dielectric permittivity ϵ ($= 4, = 6, = 10$) are used. Usually for proteins the value $\epsilon = 4$ is used, but in some cases it is not correct. Permittivity can change, especially in the case, when temperature is changed –

probably various conditions and permittivity can rise up and may be much greater than $\epsilon = 10$ [11-17, 24, 25]. Especially in the case, for example, of the dielectric anomaly of squid axon membrane near heat-block temperature which is close to the ferroelectric Curie-Weiss law, described by Leuchtag [17] and analysed by Bystrov in [11]. However, now we cannot determine these changes exactly either. Using these computed data for various permittivity values we can estimate only approximately the possible effect.

3.3.2. Discussion of piezoelectric phenomena in AA PNT

To analyse the data obtained we must first remark that all the AA PNT structures investigated are based on the long-range electrostatic interaction (following from dipole-dipole interactions of their molecular components) and including Van der Waals interactions involving the hydrogen-bonds, inherent to these structures with NH_3 , CH_3 and COO sides, especially in their zwitterionic form including water molecules. Using HyperChem tool it is easy to see how the hydrogen-bonding formation process proceeds (with direct visualization of all the molecular structures on the work-space of the monitor display screen), and how it changes during the optimization processes.

Thus, here we can see how exactly the dipole-dipole and Van der Waals interactions occur, how hydrogen bonds form, change, and affect the whole self-organization of the molecular system. The piezoelectric phenomena in similar structures are now in the focus of interest of many scientists. An example is provided by recently published papers on Piezoelectric Effects of Applied Electric Fields on Hydrogen-Bond Interactions [34], Piezoelectric Hydrogen Bonding [33] and on Role of Molecular Polarizability in Designing Organic Piezoelectric Materials [35].

Note here that the polarizability values and the electrostriction coefficients obtained in our calculations are close to data for many similar molecular structures [33 – 36, 39-41].

The most interesting is that the values of the piezoelectric coefficients obtained for various AA PNTs in our calculations are in line with the data for several hydrogen bonding systems. For example, the largest piezo-coefficient of 23 pm/V is found for

the aniline–nitrobenzene dimer, followed by 2-methyl-4-nitroaniline with 15 pm/V, and phenol-nitrobenzene with 12 pm/V [33]. The piezo-coefficient of the thiophenol-nitrobenzene (SPH-NBz) dimer computed in [34] was found to be 24.9 pm/V, greater than that of 2-methyl-4-nitroaniline (14 pm/V), the organic crystal with the largest known piezoelectric response. In [34] a mention was made that a linear correlation between piezo-coefficient and dipole moment/polarizability was established, suggesting that the dipole moment and polarizability of H-bonded systems should be considered carefully while designing new high level piezo-materials. The study of various forms of this SPH-Nbz in [34] showed that the estimated piezo-coefficients for the symmetric and anti-symmetric SPH-NBz tetramer units were found to be 20.90 pm/V and 22.20 pm/V, respectively. These values are very close to that of the SPH-NBz dimer. The authors of [34] wrote that not only the force constant and dipole moment but also the molecular polarizability of the H-bonded systems plays a crucial role in higher piezo- response. This conclusion is in full agreement with our results too and is encouraging. Therefore the data obtained confirm that many more similar H-bonded and AA tubular systems could be found with high piezo-response due to the ubiquity of hydrogen bonds in chemistry, materials and biological systems.

3.3.3. About Experimental observations of piezo-response in various AA PNT

New dipeptide nanotubes: Di-Leucine (LL), Alanine-Isoleucine (Ala-Ile, AI) and Di-Phenylalanine (Phe-Phe, FF) peptide nanotubes (PNTs) were grown and investigated. First experimental local measurement of piezoresponse parameters of LL, II, AI and FF PNTs were carried out (and will be reported in a separate paper).

The surface morphology of the material was visualized using microscope Hitachi, TM4000Plus, field-emission scanning electron microscopy with a field emission filament operating at 5-15 kV. Atomic Force Microscopy (AFM) measurements were carried out using a Veeco AFM Multimode Nanoscope (IV) MMAFM-2, Veeco microscopy. Local piezoelectric properties of the PNTs were visualized simultaneously by using Atomic Force Microscopy (AFM) in contact mode and

piezoresponse force microscopy (PFM) methods [42]. First experimental local measurement piezoresponse parameters of LL, II, AI and FF nanotubes and microcrystals are presented and analysed in comparison with modelled and computed data in [43].

4. CONCLUSIONS

In this work computational molecular modeling and quantum-chemical calculations were performed for several AA tubular structures using HyperChem tool. The systems investigated were: Leucine-Leucine (LL), Isoleucine-Isoleucine (II), Alanine-Isoleucine (AI) and Di-Phenylalanine (FF) molecular tubular structures – peptide nanotubes (PNT), which are part of the corresponding molecular crystals with a special symmetry space group and crystallographic system. The formation of these PNT proceeds as a self-assembly processes due to electrostatic dipole-dipole interaction and Van der Waals interaction with participation and reorganization of the hydrogen bonds net.

Using HyperChem tool it is possible to observe how the hydrogen-bonding formation process proceeds (with direct visualization of all the molecular structures on the work-space of the monitor display screen), and how it changes during the optimization processes. Therefore, here we can visually see how the dipole-dipole and Van der Waals interactions occur exactly, how hydrogen bonds form, change, and affect the whole self-organization of the molecular system.

The data obtained for several new self-assembled PNTs (with AA in alpha-helix conformation and L-chiral isomer) are the following:

- 1) Average polarization:
 $P(\text{LL}) = 0.036 \text{ C/m}^2$, $P(\text{II}) = 0.061 \text{ C/m}^2$, $P(\text{AI}) = 0.0802 \text{ C/m}^2$, $P(\text{FF}) = 0.023 \text{ C/m}^2$;
- 2) Piezoelectric coefficient:
 for $\varepsilon = 4$: $d_{33}(\text{LL}) = 8.0 \text{ pm/V}$, $d_{33}(\text{II}) = 10.0 \text{ pm/V}$,
 $d_{33}(\text{AI}) = 26.0 \text{ pm/V}$, $d_{33}(\text{FF}) = 35.0 \text{ pm/V}$;
 for $\varepsilon = 6$: $d_{33}(\text{LL}) = 12.0 \text{ pm/V}$, $d_{33}(\text{II}) = 15.0 \text{ pm/V}$,
 $d_{33}(\text{AI}) = 39.0 \text{ pm/V}$, $d_{33}(\text{FF}) = 52.5 \text{ pm/V}$;

These new data obtained are in line and comparable with other known values for similar molecular systems and are very important for

further investigations and practical applications.

In parallel we carried out experimental studies of these AA PNTs having prepared their samples by direct chemical synthesis and observation/measurement of surface topography and piezo-response using atomic force and piezo-response force microscopy (AFM/PFM). The data obtained by these experimental techniques confirm the computational results and demonstrate relative differences in piezo-responses of various AA PNTs. These experimental data are presented in a separate publication.

As a result, modeling and studies of various AA PNTs with electromechanical hydrogen bonds suggest that electrostatic dipole-dipole and Van der Waals interacting molecular structures will probably be ubiquitous and can be easily extended to other similar self-organizing molecular systems, using accurate quantum-chemical computational methods both semi-empirical and first-principles electronic structure calculations.

On the basis of the performed modeling and calculations (based on the self-consistent quantum-chemical calculations of the electron subsystem and taking into account electrostatic dipole-dipole interaction), we can conclude that electric-field driven molecular conformational changes in such and other similar self-assembled molecular structures will give a more substantial piezoelectric response and that deformable hydrogen bonds can be used to produce polar, self-assembled piezoelectric materials with novel desirable properties designed through computational approaches.

Thus, this work shows us an appropriate direction for further research and opens up new horizons for the analysis of these and related molecular systems, their modeling, calculations, prediction of their properties and the creation of new materials based on them.

ACKNOWLEDGMENTS

The authors are greatly thankful to Prof. Richard Leuchtag for great support, interest in this study and useful discussions, to the Russian Foundation for Basic Researches (RFBR): # 19-01-00519 A for partial support and the Portuguese Foundation for Science and Technology (FCT) for financial support: IF/00582/2015, BI (DOUTOR)/6323/2018).

REFERENCES

- [1] A. L. Lehninger, *Biochemistry. The Molecular Basis of Cell Structure and Function*. New York: Worth Publishers, Inc. (1972).
- [2] M. E. Lines and A. M. Glass, *Principles and Applications of Ferroelectrics and Related Materials*. Oxford: Clarendon Press (1977).
- [3] A. C. Mendes, E. T. Baran, R. L. Reis, H. S. Azevedo. Self-assembly in nature: using the principles of nature to create complex nanobiomaterials. *Wiley Interdiscip. Rev. Nanomed. Nanobiotechnol.* **5(6)**, 582–612 (2013).
- [4] Y. Iitaka, The crystal structure of β -glycine. *Acta Crystallogr.* **13**, 35–45 (1960); Y. Iitaka, The crystal structure of γ -glycine. *Acta Crystallogr.* **14**, 1–10 (1961).
- [5] E. Seyedhosseini, M. Ivanov, V. Bystrov, I. Bdikin, P. Zelenovsky, V. Ya. Shur, A. Kudryavtsev, E.D. Mishina, A. S. Sigov, A. L. Kholkin. Growth and Nonlinear Optical Properties of Glycine Crystals Grown on Pt Substrates. *Crystal Growth & Design*. **14(6)**, 2831-2837 (2014).
- [6] V.S. Bystrov, E. Seyedhosseini, I.K. Bdikin, S. Kopyl, A.L. Kholkin, S.G. Vasilev, P.S. Zelenovskiy, D.S. Vasileva & V.Ya. Shur. Glycine nanostructures and domains in betaglycine: Computational modeling and PFM observations. *Ferroelectrics*. **496**, 28–45 (2016).
- [7] M. R. Ghadiri, J. R. Granja, R. A. Milligan, D. E. McRee, N. Hazanovich N. Self assembling organic nanotubes based on cyclic peptide architecture. *Nature*. **366**, 324–327 (1993).
- [8] C. H. Görbitz. Nanotube formation by hydrophobic dipeptides. *Chem. Eur. J.* **7**, 5153–5159 (2001).
- [9] V. S. Bystrov, I. Bdikin, A. Heredia, R. C. Pullar, E. Mishina, A. Sigov and A. L. Kholkin, Piezoelectric nanomaterials for biomedical applications: piezoelectricity and ferroelectricity in biomaterials: from proteins to self-assembled peptide nanotubes. In: G. Ciofani and A. Menciassi, eds. *Piezoelectric nanomaterials for biomedical applications.. Berlin Heidelberg, Springer-Verlag*. 187-212 (2012).
- [10] V. S. Bystrov, E. Seyedhosseini, S. Kopyl, I. K. Bdikin, and A. L. Kholkin. Piezoelectricity and ferroelectricity in biomaterials: Molecular modeling and piezoresponse force microscopy measurements. *J. Appl. Phys.* **116(6)**, 066803 (2014).
- [11] V. S. Bystrov. Computer Simulation Nanostructures: Bioferroelectric Peptide Nanotubes. Bioferroelectricity: Peptide Nanotubes. Saarbruecken: LAP Lambert Academic Publishing. *OmniScriptum GmbH & Co. KG*. (2016).
- [12] V. S. Bystrov, E. Paramonova, I. Bdikin, S. Kopyl, A. Heredia, R. Pullar, A. Kholkin. BioFerroelectricity: Diphenylalanine Peptide Nanotubes Computational Modeling and Ferroelectric Properties at the Nanoscale. *Ferroelectrics*, **440 (01)**, 3 – 24 (2012).
- [13] H. R. Leuchtag, Voltage-Sensitive Ion Channels: Biophysics of Molecular Excitability, *Dordrecht: Springer* (2008).

- [14] H. R. Leuchtag and V. S. Bystrov, Theoretical models of conformational transitions and ion conduction in voltage-dependent ion channels: Bioferroelectricity and superionic conduction. *Ferroelectrics*, **220** (3-4), 157-204 (1999).
- [15] V. S. Bystrov, H. R. Leuchtag, Bioferroelectricity: Modeling the transitions of the sodium channel. *Ferroelectrics*, **155**, 19-24 (1994).
- [16] H. R. Leuchtag, Bioferroelectricity in models of voltage-dependent ion channels. *Ferroelectrics*, **236**, 23-33 (2000).
- [17] H. R. Leuchtag, Fit of the dielectric anomaly of squid axon membrane near heat-block temperature to the ferroelectric Curie-Weiss law, *Biophys. Chem.*, **53**, 197-205 (1995).
- [18] B. Coste, B. Xiao, J. S. Santos, R. Syeda, J. Grandl, K. S. Spencer, S. E. Kim, M. Schmidt, J. Mathur, A. E. Dubin, M. Montal, and A. Patapoutian, "Piezo proteins are pore-forming subunits of mechanically activated channels. *Nature*. **483**(7388), 176 (2012).
- [19] S. E. Kim, B. Coste, A. Chadha, B. Cook, and A. Patapoutian, The role of Drosophila Piezo in mechanical nociception. *Nature*. **483**, 209 (2012).
- [20] S. Horiuchi, R. Kumai and Y. Tokura, Hydrogen-bonding molecular chains for high-temperature ferroelectricity. *Adv. Mater.* **23**, 2098 (2011).
- [21] A. Heredia, I. Bdikin, S. Kopyl, E. Mishina, S. Semin, A. Sigov, K. German, V. Bystrov, A. L. Kholkin. Temperature-driven phase transformation in self-assembled diphenylalanine peptide nanotubes. Fast Track Communication. *J. Phys. D: Appl. Phys.* **43**, 462001 (2010).
- [22] I. Bdikin, V. Bystrov, I. Delgadillo, J. Gracio, S. Kopyl, M. Wojtas, E. Mishina, A. Sigov and A. L. Kholkin. Polarization switching and patterning in self-assembled peptide tubular structures. *J. Appl. Phys.* **111**, 074104 (2012).
- [23] V. S. Bystrov, S. A. Kopyl, P. Zelenovskiy, O. A. Zhulyabina, V. A. Tverdislov, F. Salehli, N. E. Ghermani, V. Ya. Shur & A. L. Kholkin. Investigation of physical properties of diphenylalanine peptide nanotubes having different chiralities and embedded water molecules. *Ferroelectrics*, **525**, 168-177 (2018).
- [24] K. Yoshino, T. Sakurai. Ferroelectric liquid crystals and their chemical and electrical properties. In: Goodby, J.W. et al, editors. *Ferroelectric Liquid Crystals: Principles, Properties and Applications*. Gordon and Breach: Philadelphia, 317-363 (1991).
- [25] A. Chen, C.- D. Poon, T. Dingemans, and E. T. Samulski. Ferroelectric liquid crystals derived from isoleucine. II. Orientational ordering by carbon-13 separated local field spectroscopy. *Liquid Crystals*. **24**, 255-262 (1998).
- [26] V. S. Bystrov, P. S. Zelenovskiy, A. S. Nuraeva, S. Kopyl, O. A. Zhulyabina, V. A. Tverdislov. Molecular modeling and computational study of the chiral-dependent structures and properties of the self-assembling diphenylalanine peptide nanotubes. *J. Mol. Mod.* **25**, 199 (2019).
- [27] C. H. Gorbitz. Hydrophobic dipeptides: the final piece in the puzzle. *Acta Cryst.*, **B74**, 311- 318 (2018).
- [28] HyperChem: Tools for Molecular modeling (release 8). Gainesville: Hypercube, Inc. (2002).
- [29] V. V. Lemanov, S. N. Popov, G. A. Pankova, Piezoelectric properties of crystals of some protein aminoacids and their related compounds, *Phys. Sol. Stat.*, **44**, 1929-1935 (2002).
- [30] V. V. Lemanov, S. N. Popov, G. A. Pankova, Protein amino acid crystals: Structure, symmetry, physical properties, *Ferroelectrics*. **285**, 581-590 (2003).
- [31] V. S. Bystrov, E. Seyedhosseini, I. Bdikin, S. Kopyl, S. M. Neumayer, J. Coutinho, A. Kholkin, BioFerroelectricity: Glycine and Thymine nanostructures computational modeling and ferroelectric properties at the nanoscale. *Ferroelectrics*. **475**(1), 107-126 (2015).
- [32] V. S. Bystrov. Photo-Ferroelectricity in diphenylalanine peptide nanotube. *Computational Condensed Matter*. **14**, 94-100 (2018).
- [33] K. A. Werling, M. Griffin, G. R. Hutchison and D. S. Lambrecht, Piezoelectric Hydrogen Bonding: Computational Screening for a Design Rationale. *J. Phys. Chem. A*. **118**, 7404-7410 (2014).
- [34] K. A. Werling, G. R. Hutchison, D. S. Lambrecht, Piezoelectric Effects of Applied Electric Fields on Hydrogen-Bond Interactions: First-Principles Electronic Structure Investigation of Weak Electrostatic Interactions. *J. Phys. Chem. Lett.* **4**(9), 1365-1370 (2013).
- [35] A. A. Gagrai, V. R. Mundlapati, D. K. Sahoo, H. Satapathy, and H. S. Biswal. The Role of Molecular Polarizability in Designing Organic Piezoelectric Materials. *Chemistry Select.* **1**, 4326 - 4331 (2016).
- [36] R. E. Newnham, V. Sundar, R. Yimnirun, J. Su, Q. M. Zhang, Electrostriction: Nonlinear Electromechanical Coupling in Solid Dielectrics. *J. Phys Chem B*. **101**, 10141-10150 (1997).
- [37] A. L. Kholkin, K. G. Brooks and N. Setter, Electromechanical properties of SrBi₂Ta₂O₉ thin films, *Appl. Phys. Lett.*, **71**(14), 2044 (1997).
- [38] V. S. Bystrov, I. K. Bdikin and Budhendra Singh, Piezoelectric and ferroelectric properties of various amino acids and dipeptides structures: molecular modeling and experiments. In: I. Bdikin, Budhendra Singh, Raul Simões, eds. 2nd International Conference on Nanomaterials Science and Mechanical Engineering. *Book of Abstracts. Aveiro, UA Editora, Universidade de Aveiro*, **44** (2019).
- [39] K. Yamada, A. Saiki, H. Sakae, S. Shingubara, and T. Takahagi, Study of a dielectric constant due to electronic polarization using a semiempirical molecular orbital method. *Jpn. J. Appl. Phys.* **40**, 4829-4836 (2001).
- [40] V. S. Bystrov, et al. Molecular modelling of the piezoelectric effect in the ferroelectric polymer poly(vinylidene fluoride) (PVDF). *J. Mol. Mod.*, **19**, 3591-3602 (2013).
- [41] V. S. Bystrov, Piezoelectricity in the ordered monoclinic hydroxyapatite. *Ferroelectrics*, **475**, iss.1, 148-153 (2015).

- [42] A. Roelofs, T. Schneller, K. Szot, R. Waser. Piezoresponse force microscopy of lead titanate nanograins possibly reaching the limit of ferroelectricity. [*Applied Physics Letters*, **81** \(27\), 5231-5233 \(2002\).](#)
- [43] Budhendra Singh, V. S. Bystrov, Nuno Almeida, I.K. Bdkin, Local piezoelectric properties of Di-Leucine and Alanine-Isoleucine dipeptides nanotubes. - in print.

Thermally activated processes and bias field effects on the electrical properties of BiFeO₃ thin films

Saulo Portes dos Reis¹, Fernando Brondani Minussi² and Eudes B. Araújo³

¹ Federal Institute of Education, Science and Technology of São Paulo, 15503-110 Votuporanga, Brazil, spdreis@ifsp.edu.br

² Department of Physics and Chemistry, São Paulo State University, 15385-000 Ilha Solteira, Brazil, fminussi@gmail.com

³ Department of Physics and Chemistry, São Paulo State University, 15385-000 Ilha Solteira, Brazil, eudes.borges@unesp.br

Received 13 December 2019; accepted 26 February 2020; published online 10 March 2020

ABSTRACT

This work reports the temperature and electric field effects on the electrical properties of BiFeO₃ thin films. The increase in temperature promotes an increase in the dielectric permittivity of the studied film in the range of 100 Hz to 1 MHz, with a dielectric dispersion at the lower frequencies (~ 100 Hz), but no pronounced effects of the electric field on dielectric permittivity in the same frequency range were observed. The effects of temperature and electric on the electrical conductivity were also studied. Based on the obtained activation energy $E = 0.40$ eV, the conduction mechanism in the studied BiFeO₃ film was associated to the first ionization of oxygen vacancies.

1. INTRODUCTION

Known by a large ferroelectric polarization observed in thin films form [1], the BiFeO₃ (BFO) is a multiferroic material and as a promising material for the development of new spintronics devices based on the control of magnetization by an electric field [2]. On the other hand, due to a large leakage current at room temperature, the ferroelectric behavior of BiFeO₃ has proved to be a very difficult task from an experimental point of view, which further limits practical technological applications of BFO in the announced new multiferroic devices. In this scenario, grain boundaries in polycrystalline materials and impurities in single crystals are important points to consider as electrical measurements are very sensitive to these defects. Because these imperfections are more evident in polycrystalline samples than in BiFeO₃ single crystals, it is natural that higher leakage currents in polycrystalline thin films generally prevent the

application of high electric fields, making it difficult to measure a well-defined hysteresis loop. Thus, controlling defects in thin films of BFO, among other characteristics, has motivated continuous studies on the electrical properties of this multiferroic.

Electrical characterizations have been used to better understand the mechanisms behind the leakage current in BiFeO₃ thin films produced by different techniques and to understand the temperature and electrical field effects on these properties. The combination of complex impedance spectroscopy and electrical modulus spectroscopy has shown to be a powerful tool to study the dielectric relaxations of BiFeO₃ ceramics and thin films to infer about the influence of oxygen vacancies on the leakage current and its dielectric properties [3], the effects of Mn substitution on its electrical properties [4], the suppression of grain boundary relaxation in BFO films [5], and others. Usually, the non-Debye relaxation in multiferroic

thin films [6] or polycrystalline materials [7] is described in terms of the Cole-Cole model and subsequent generalizations to reveals the contributions of the grain, grain boundary and electrodes. However, a more realistic brick layer model can be alternatively used to describe the effects of inhomogeneous gains in electronic ceramics in terms of probability distributions [8], since the Cole-Cole model is not able to fit our data at lower frequencies. In this case, some effects that are not distinguished by the Cole-Cole model in the popular Nyquist diagram and other representations can be revealed using this statistical treatment [9]. These approaches indicate the importance of the electrical characterization as investigative tool to examine the dielectric relaxation and ac conductivity of BFO thin films for both academic and application point of view. In this article, we report the use of impedance formalism to discriminate thermally and electric field activated processes on the conductivity and permittivity of BiFeO₃ thin films prepared by chemical route.

2. FUNDAMENTALS AND BACKGROUND

2. 1. Impedance spectroscopy

Impedance spectroscopy is a technique widely used in the analysis of electrical properties of ceramics, ferroelectrics and mixed conductor [10]. The technique consists of placing the sample between two electrodes, forming a capacitor-like sample, then applying a variable voltage $V(t)$ and measuring the current obtained, $i(t)$, and its lag with respect to $V(t)$. In order to extract relevant physical parameters such as the electric conductivity and electric permittivity, it is essential to propose an equivalent circuit that is able to describe the experimental data [11]. To do this, we believe that a good mathematical understanding of the process and reasons for using impedance analysis is required.

Considering $V(t)$ the applied voltage and $i(t)$ the measured current, the complex impedance (Z^*) and complex admittance (Y^*) (the reciprocal of impedance) are defined as follow [12]:

$$Z^* = \frac{F\{V(t)\}}{F\{i(t)\}} \text{ and } Y^* = \frac{F\{i(t)\}}{F\{V(t)\}} \quad (1)$$

where $F\{\}$ denotes the Fourier transform operator. From equation (1) we obtain that the impedance of a resistor with a resistance R and a capacitor of capacitance C are respectively given by $Z_R^* = R$ and $Z_C^* = (j\omega C)^{-1}$, where ω is the angular frequency of the applied signal and $j^2 = -1$. The great advantage of defining impedance through Fourier transforms lies in the operator linearity, which imposes that the impedance association has the same rules as the resistor associations.

Non-localized diffusion processes can be described by a circuit constructed by a parallel association between a resistor and a capacitor [13], so the impedance and admittance of these processes are respectively given by:

$$Z^* = \frac{R}{1 + j\omega RC} \text{ and } Y^* = \frac{1}{R} + j\omega C \quad (2)$$

where the RC product is named as relaxation time represented by τ . Since S and l are the sample geometrical parameters (area and thickness, respectively), the above equations indicate that the electrical conductivity and permittivity are constant, i.e., do not depend on ω . The representation given above is not accurate when the dynamic processes acting on the system in question have very close distribution times, which causes a dispersion in both conductivity and permittivity. In this case we should consider a distribution of relaxation times [13].

2. 2. Relaxation times distribution: discrete case

It is commonly recognized that the impedance response of a particular material can be simulated by more than one equivalent electrical circuit to describe its bulk and grain boundaries contributions, but researchers tend to use the most appropriate circuit to explain their results in a realistic scenario without inconsistencies. To represent different conductivity processes in a given material, the equivalent circuit illustrated in Figure 1 can be used.

We note that each RC component of the circuit has a characteristic relaxation time. Considering that $\tau_k = R_k C_k$, it follows:

$$Z^* = \sum_{k=1}^n \frac{R_k}{1 + j\omega\tau_k} \text{ and } Y^* = \left(\sum_{k=1}^n \frac{1}{\frac{1}{R_k} + j\omega C_k} \right)^{-1} . \quad (3)$$

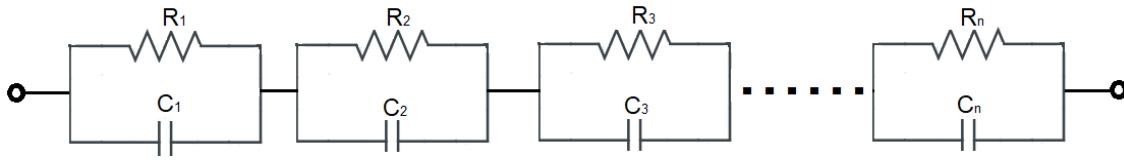


Figure 1. Representation of n parallel RC circuits in associated in series to represent different relaxation times.

The admittance equation allows us to obtain the profile of the dispersions of the real components of conductivity and permittivity, respectively:

$$\sigma'(\omega) = \frac{\Sigma\left(\frac{\sigma_k}{\sigma_k^2 + \omega^2 \epsilon_0^2 \epsilon_k^2}\right)}{\left[\Sigma\left(\frac{\sigma_k}{\sigma_k^2 + \omega^2 \epsilon_0^2 \epsilon_k^2}\right)\right]^2 + \omega^2 \left[\Sigma\left(\frac{\epsilon_0 \epsilon_k}{\sigma_k^2 + \omega^2 \epsilon_0^2 \epsilon_k^2}\right)\right]^2} \tag{4}$$

$$\epsilon'(\omega) = \frac{\Sigma\left(\frac{\epsilon_k}{\sigma_k^2 + \omega^2 \epsilon_0^2 \epsilon_k^2}\right)}{\left[\Sigma\left(\frac{\sigma_k}{\sigma_k^2 + \omega^2 \epsilon_0^2 \epsilon_k^2}\right)\right]^2 + \omega^2 \left[\Sigma\left(\frac{\epsilon_0 \epsilon_k}{\sigma_k^2 + \omega^2 \epsilon_0^2 \epsilon_k^2}\right)\right]^2} \tag{5}$$

On the limit for low frequencies:

$$\lim_{\omega \rightarrow 0} \sigma(\omega) = \sigma_{dc} = \frac{1}{\frac{1}{\sigma_1} + \frac{1}{\sigma_2} + \dots + \frac{1}{\sigma_n}} \quad \text{and} \quad \lim_{\omega \rightarrow 0} \epsilon(\omega) = \frac{\frac{\epsilon_1}{\sigma_1^2} + \frac{\epsilon_2}{\sigma_2^2} + \dots + \frac{\epsilon_n}{\sigma_n^2}}{\left(\frac{1}{\sigma_1} + \frac{1}{\sigma_2} + \dots + \frac{1}{\sigma_n}\right)^2} \tag{6}$$

and, for high frequencies:

$$\lim_{\omega \rightarrow +\infty} \sigma(\omega) = \frac{\frac{\sigma_1}{\epsilon_1^2} + \frac{\sigma_2}{\epsilon_2^2} + \dots + \frac{\sigma_n}{\epsilon_n^2}}{\left(\frac{1}{\epsilon_1} + \frac{1}{\epsilon_2} + \dots + \frac{1}{\epsilon_n}\right)^2}, \quad \text{and} \quad \lim_{\omega \rightarrow +\infty} \epsilon(\omega) = \epsilon_r = \frac{1}{\frac{1}{\epsilon_1} + \frac{1}{\epsilon_2} + \dots + \frac{1}{\epsilon_n}} \tag{7}$$

Equations (6) and (7) indicate that low frequency electrical conductivity (σ_{dc}) is dominated by the lowest conductivity element, but at high frequencies the conductivity shows an intrinsic permittivity dependence. Similarly, the electric permittivity is influenced by conductivity in low

frequencies and is dominated by the element of lowest permittivity at high frequencies.

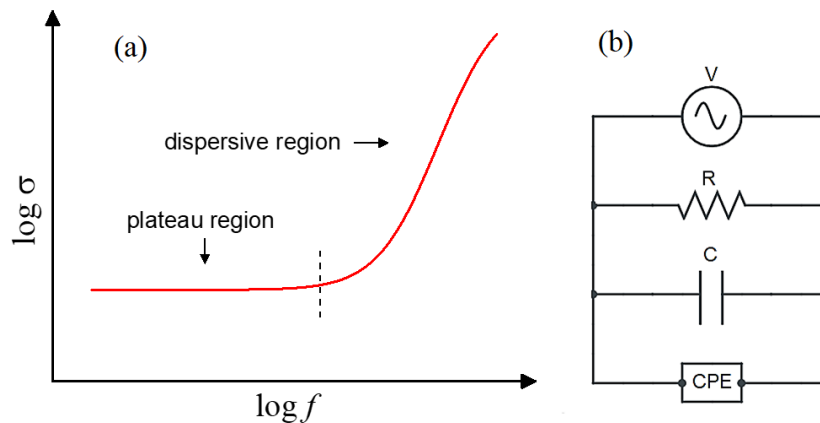


Figure 2. (a) Typical log–log real conductivity (σ) versus frequency relationship at a given temperature for conductive materials. (b) The used model to describe the conductivity in (a). times.

2. 3. Relaxation times distribution: continuous case

Switching to the continuous case requires a density function that represents the distribution of resistor and capacitance values. In this case, the impedance equation is given by:

$$Z^* = \int_0^{\infty} \frac{G(\tau) d\tau}{1 + j\omega\tau}, \quad (8)$$

where $G(\tau)$ represents the total resistance over a relaxation time interval $d\tau$. The solution of this integral can be difficult to obtain even for simple functions (as seen in [14]). However, in addition to the mentioned elements of the circuit, the inclusion of constant phase elements (CPE's), such as $Z_{CPE}^* = (jA\omega)^{-n}$, representing the departures from Debye-like ideality of each component, describes the distribution of relaxation times with the distribution parameter A , as proposed by Cole-Cole [15]. Since an ideal Debye-like response was never obtained, the impedance response cannot be treated in terms of simple parallel RC elements. Thus, the inclusion of the CPE element is comprehensive to fit the experimental frequency dependence of real conductivity, as shown in Figure 2(a). The CPE element describes the so-called Jonscher's law [16]. In summary, the RC-CPE circuit shown in Figure 2(b) is used to describe the grain boundaries impedance in polycrystals materials.

Considering the model described by the electrical circuit shown in Figure 2(b), the real

components of the electric conductivity and the electric permittivity are given by:

$$\sigma'(\omega) = \sigma_{dc} + A' \omega^n \cos\left(\frac{n\pi}{2}\right) \quad (9)$$

$$\epsilon'(\omega) = \epsilon_r + \frac{A'}{\epsilon_0 \omega^{1-n}} \sin\left(\frac{n\pi}{2}\right), \quad (10)$$

where $A' = (Al)/S$, $\sigma_{dc} = l/(RS)$ and $\epsilon_r = (Cl)/(\epsilon_0 S)$. It should be noted that the conductivity equation is in the form $\sigma(\omega) = \sigma_{dc} + B\omega^n$, as attributed by Jonscher [16]. These two equations above are in agreement with what was discussed in the discrete case, as the electric conductivity converges at low frequencies, while dielectric permittivity converges at high frequencies. Moreover, the term A' contained in the CPE is responsible for accounting the dispersion of both the resistance (conductivity) and the capacitance (permittivity) of a sample, so we can infer that the CPE simplifies the expressions containing the quadratic terms of electric permittivity and electric conductivity.

2.4. Thermally activated conductivity

Many ceramic materials conduct electricity through ion migration [17]. This ionic conductivity involves the migration of charge carriers (ions) over long distances and, being this process thermally activated, then its temperature dependence is typically described by an Arrhenius type expression such as [18]:

$$\sigma_{dc} = \sigma_0 \exp\left(\frac{-E_a}{kT}\right), \quad (11)$$

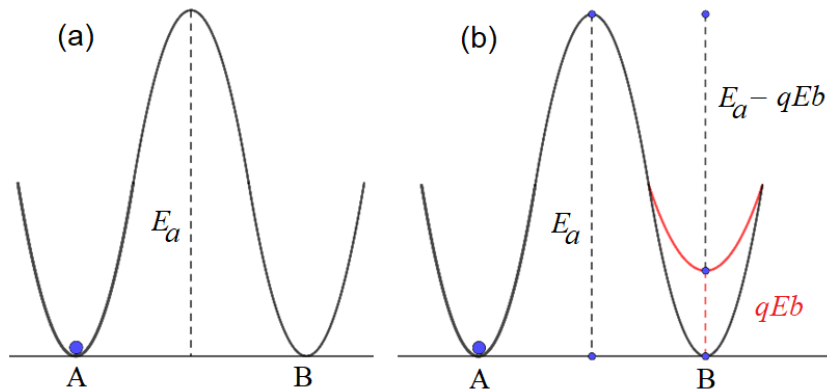


Figure 3. Energy levels before (a) and after (b) the application of a bias electric field E . In this figure, E_a is the activation energy, q the charge carrier and b the jump distance.

where σ_0 is a pre-exponential parameter, k is the Boltzmann constant and E_a the activation energy of a given ionic conduction process. The activation energy for ionic conduction, as illustrated in Figure 3(a), consists of the energy barrier of the lowest resistance path [9]. In order to a charge carrier to migrate, a minimum energy corresponding to this activation energy must be provided. In the absence of an energy difference between the positions given by A and B in Figure 3(a), there is no net movement of the charge carriers in a given direction, *i.e.*, the probability of jump from A to B is equal to the probability of jump from B to A. However, once an electric potential difference is applied, as shown in Figure 3(b), an electric field arises and causes an imbalance between the energies at positions A and B.

Considering the presence of a bias electric field E , the energy difference (ΔU) between positions A and B can be given by:

$$\Delta U = qEb, \quad (12)$$

where q is the carrier charge and b is the distance between A and B, which are the lowest energies of the respective potential wells (or the equilibrium points). Taking this energy configuration, it is observed that the potential barrier for a jump from A to B is different from that of the jump from B to A, resulting in an imbalance of the jump probability. In other words, the bias electric field disturbs the initially random thermal motion, increasing the probability of transition in the direction of field application to a cation and in the reverse direction to an anion. So, in the presence of a bias electric

field, there is a decreasing of the potential barrier for a jump from B to A. Calling this decreasing as E_{eff} barrier, it follows that for a thermally activated process:

$$\sigma_{dc} = \sigma_0 \exp\left(\frac{-E_{eff}}{kT}\right). \quad (13)$$

Observing that $E_{eff} = E_a - \Delta U = E_a - qEb$, it follows that:

$$\sigma_{dc} = \sigma_0 \exp\left(\frac{-E_a + qEb}{kT}\right). \quad (14)$$

From Equations (13) and (14) it is observed that $\ln(\sigma_{dc})$ decreases with the reciprocal temperature and increases with the bias electric field, resulting essentially in the same response, which is the conductivity increasing of an ionic process. However, it should be emphasized that for a rise in temperature, this behavior is a consequence of the higher energy available to the system to overcome the energy barrier of an ionic conduction process, which is, in a first approximation, constant with the temperature. In turn, under an applied electric field the energy barrier will change resulting in a smaller "effective" activation energy. According to the Equation (14), it should be noted that the ionic mobility is not null for a situation where there is not an applied electric field, but, for a hypothetical absolute zero condition, the migration would not be possible. In other words, we can interpret that the role of temperature is to provide mobility to charge carriers, while the electric field provides a preferential direction of migration. For a such temperature, Equation (14) can be rewritten to describe the electric field dependence such as:

$$\ln(\sigma_{dc}) = a_1 + a_2 E, \quad (15)$$

where $a_1 = \ln(\sigma_0) - E_a/kT$ and $a_2 = qb/kT$.

3. EXPERIMENTAL PROCEDURE

In the present work, BiFeO₃ thin films were prepared by a chemical solution route dissolving appropriate amounts of bismuth nitrate pentahydrate Bi(NO₃)₃.5H₂O (Sigma-Aldrich, 99.9%) and iron nitrate nonahydrate Fe(NO₃)₃.9H₂O (Sigma-Aldrich, 99.9%) into a solution composed by 1 mL of 2-methoxyethanol (Sigma-Aldrich, 99.9%) and 5 mL of glacial acetic acid (Sigma-Aldrich, 99.9%), at 50°C under magnetic stirring for 10 min. After complete homogenization, the temperature of the solution was raised to 80°C and kept under stirring for 30 min. Finally, after cooling to room temperature, 3 mL of glacial acetic acid was added to obtain a 0.16 M solution after filtering it using a microfiber filter paper.

Films of the precursor solution were deposited (4 depositions) on Pt/TiO₂/SiO₂/Si(100) substrates by spin-coating at 5000 rpm for 30 seconds. After the solution deposition, the films were placed directly on a hot-plate at ~ 200°C for 5 min to remove water, and then annealed in an electric furnace at 300°C for 30 min to remove organics. By following the same procedure, additional layers were deposited on the previously annealed film to increase its thickness. Next, the films were crystallized in air at 600°C for 40 min and finally post annealed at 600°C for 5 hours in O₂ atmosphere. The thickness of the final film is found to be ~ 500 nm. For electrical measurements,

circular Au top electrodes of 0.30 mm diameter were sputtered on the film surfaces by using a shadow mask. An Agilent 4284A LCR meter was used to measure the complex impedance in the frequency, temperature and bias electrical field ranges of 100 - 10⁶ Hz, 335 - 420 K (with no bias field) and 0 - 22 kV.cm⁻¹ (room temperature), respectively.

4. RESULTS AND DISCUSSION

Figure 4 shows the variation of real dielectric permittivity (ϵ') of the studied BiFeO₃ thin film in the frequency range of 100 Hz to 1 MHz, at different temperatures (a) and bias electric field (b). In Figure 4(a), the value of permittivity falls with frequency increasing, but at the lower frequency it reaches higher values. In other words, at frequencies lower than 10 kHz a pronounced dielectric dispersion is observed while at higher frequencies the permittivity tends to a frequency independent value ($\epsilon_\infty \sim 26$). On the other hand, at higher temperatures the dielectric permittivity increases, such that the temperature effects are less pronounced at higher frequencies than at low frequencies, where a dielectric dispersion is observed, as shown in Figure 4(a). In contrast to the effects of temperature, similar dielectric dispersions on dielectric permittivity were not observed by applying different external dc electric field, as shown in Figure 4 (b). The dielectric permittivity behavior in this figure was essentially the same for different electric field in the studied frequency range and, under the electric field effects, the frequency independent permittivity tends to $\epsilon_\infty \sim 36$.

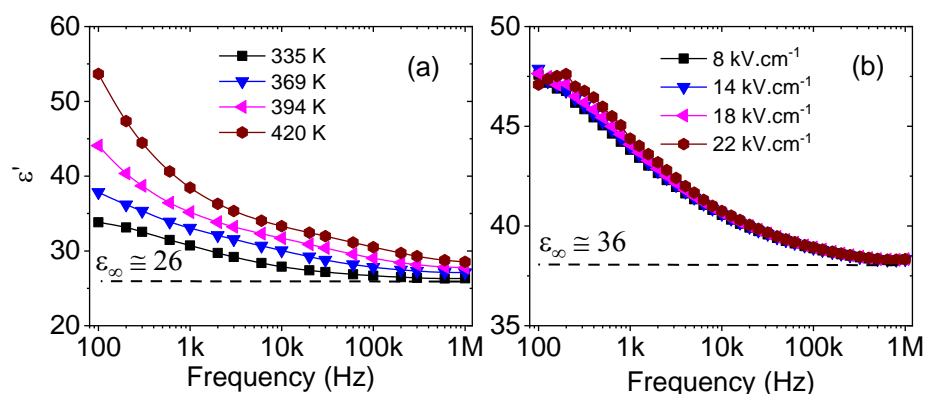


Figure 4. Frequency dependence of the real permittivity for BiFeO₃ thin film obtained from impedance measurements at (a) different temperatures and (b) different bias electric field.

The presence of different polarizations, such as ionic, dipolar and space-charge, may be responsible for higher permittivity values at lower frequencies, but at higher frequencies some of them do not follow the alternating field, so their contribution to permittivity decrease or disappear resulting in lower permittivity values. It is well known that electronic polarization predominates in the high-frequency region [19]. The dielectric dispersion observed at low frequencies can be explained by the greater interference of grain effects over grain boundary effects, which is attributed to Maxwell–Wagner type of interfacial polarization in accordance with Koop's phenomenological theory [20]. The presence of space charge polarization at the grain boundaries generates a potential barrier responsible for the observed high values of the real part of permittivity. The decrease of the real part of permittivity at higher frequencies can be understood if we consider that low resistive grains are separated by grain boundaries with lower conductivity in dielectric, as shown in Equation (7). Thus, regarding the temperature effects, it is expected that dielectric permittivity increases with increasing temperature, and this increase is higher in the dielectric dispersion at lower frequencies, as

demonstrates Equation (6) and as shown in Figure 4(a). This dielectric dispersion at low temperatures agree with those observed in typical ferroelectrics [21], as well as for BiFeO₃ thin films prepared by chemical solution deposition method [22]. As a result of the applied electric field, a localized accumulation of charges occurs leading to the interfacial polarization [23]. In Figure 4(b), no pronounced effects of bias electric field on dielectric permittivity suggest that the DC electric field causes a saturation of spatial charge. The difference between independent permittivity values is attributed to difference between relaxation times in the two process. As mentioned before, we can define $\tau = RC$ as the relaxation time, which leads to:

$$\tau = RC = \epsilon_0 \epsilon_r \frac{1}{\sigma_{DC}} . \quad (16)$$

Therefore, a change in the relaxation time causes a change in the relative permittivity. This difference probably due to a higher concentration of special loads caused by applying a DC field.

Figure 5(a) shows the frequency dependence of the conductivity while Figure 5(b) shows Nyquist plots of Z' versus Z'' of the studied BiFeO₃ thin film at different temperatures (top) and different bias

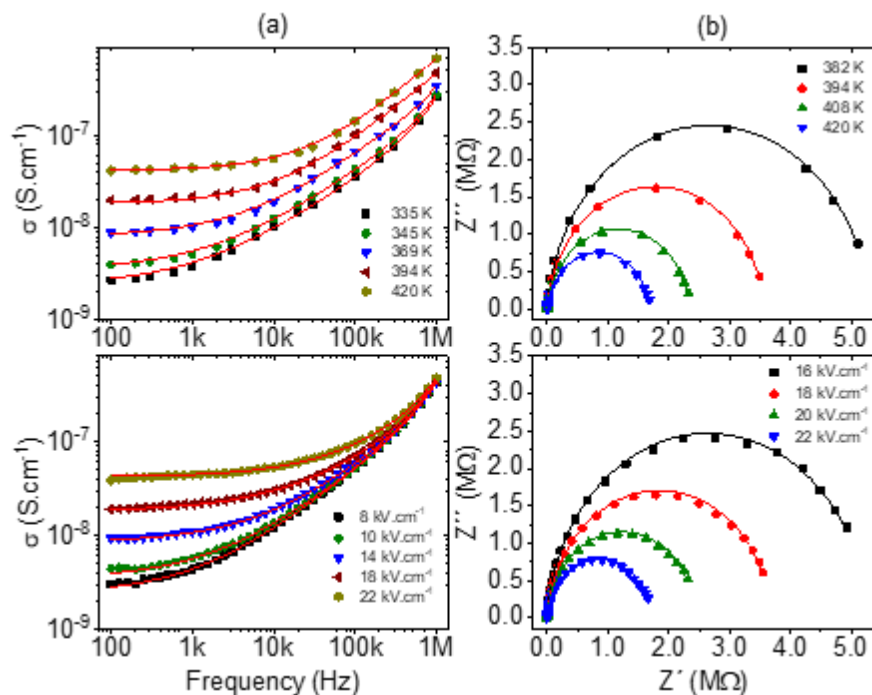


Figure 5. (a) Frequency dependence of the conductivity and (b) Nyquist plots of Z' versus Z'' for BiFeO₃ thin film at different temperatures (top) and different bias electric field (bottom). Symbols are experimental data and lines are theoretical fits (R-C-CPE model).

electric field (bottom). Lines in Figure 5(a) top are theoretical fits from Jonscher model described in Equation (9), which are in good agreement with experimental data. It was observed in Figure 5(a) that the temperature and electric field effects on electrical conductivity at low frequencies (σ_{dc}) were essentially the same. In other words, the σ_{dc} increases when both temperature and electric field increases, as predicted by Equations (11) and (14). However, the conductivity shows a temperature dependence at higher frequencies while the high-frequency conductivity is electric field independent. Nyquist plots in Figure 5(b) shows the same temperature and electric field effects in another perspective. Since the diameter of the semicircles in the impedance diagram represents the resistance, the decrease observed in the semicircles with increasing temperature and electric field corroborates the increase in conductivity observed in Figure 5(a).

From theoretical fits to the experimental data shown in Figure 5(a) at the top, the obtained dc conductivities were plotted in Figure 6(a) as a function of the temperature. Based on linear fit in this figure, the obtained activation energy was 0.40

eV. This activation energies are in good agreement with those values reported for BFO thin films prepared by rf sputtering [24]. In general, activation energies around 0.28 eV are associated to the first ionization of oxygen vacancies in perovskite structure of Bi-doped SrTiO₃ ceramics [25]. Thus, the obtained activation energy in the present work suggests that the conduction mechanism in studied BiFeO₃ can be associated to the first ionization of oxygen vacancies. Considering the temperature and electric field that led to the same dc electric conductivity in the sample, as example the data obtained at 334.8K had the same electric conductivity as the obtained with a field of 8 kV.cm⁻¹ and so on, dc conductivity of the BiFeO₃ thin film was plotted in Figure 6(b) as a function of electric field, where a slope of 0.20 was obtained. On the other hand, the linear behavior in Figure 6(c) shows the temperature as a function of the electric field. Since the slope in this curve is 6.12, we can conclude that an increase of the 1 kV.cm⁻¹ should result in the same variation in the dc conductivity of an increase of 6.12 K in temperature.

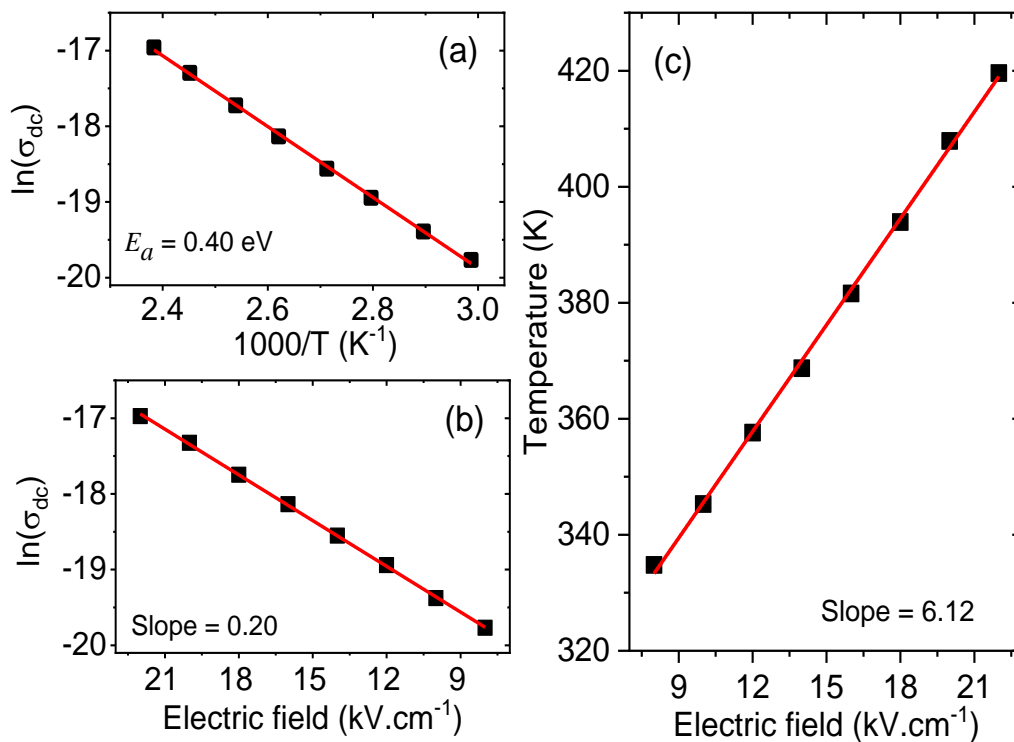


Figure 6. DC conductivity as a function of (a) reciprocal temperature and (b) electric field for BiFeO₃ thin film. (c) Electric field dependence of temperature. Red lines are linear fits.

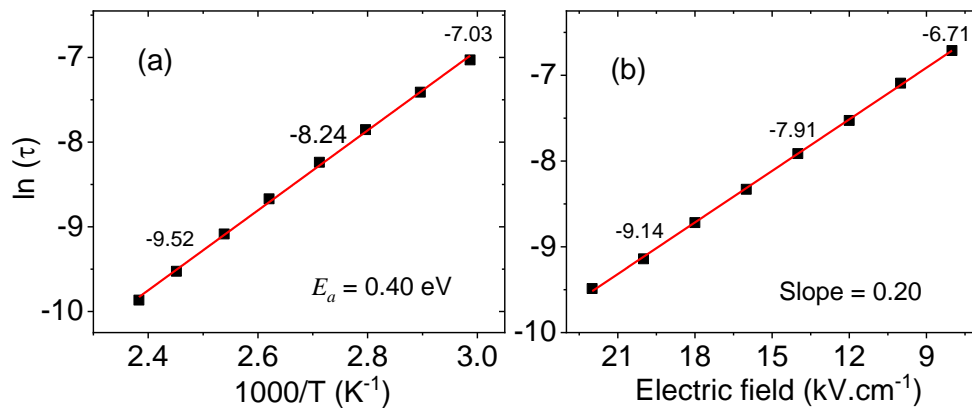


Figure 7. Relaxation time as a function of (a) reciprocal temperature and (b) electric field for BiFeO₃ thin film.

Finally, relaxation times as a function of temperature and bias electric field were plotted in Figures 7(a) and 7(b), respectively. Although the activation energy of 0.40 eV and the slope of 0.2 in these figures were the same values as obtained in Figures 6(a) and 6(b), point values presented in Figures 7(a) and 7(b) indicate that a difference in the value of the relaxation times exists a difference in the value of the relaxation times, although the dc conductivity is the same. This fact was first identified in the Figure 5(a), where the temperature and electric field effects on conductivity are different at higher frequencies. Equation (7) shows that the conductivity is affected by permittivity at high frequencies, indicating that the difference between relaxation times occurs because the electric field and the temperature change the capacitance of the sample in a different manner.

5. CONCLUSIONS

The temperature and electric field effects on the electrical properties of BiFeO₃ thin film were studied. The dielectric permittivity of the studied BiFeO₃ film increases by increasing the temperature and this increasing is higher in the dielectric dispersion at lower frequencies, while no pronounced effects of bias electric field on dielectric permittivity were observed. The conductivity at low frequencies (σ_{dc}) increases when both temperature and electric field increases, but the conductivity shows a temperature dependence at higher frequencies while the high-frequency conductivity is electric field independent. The obtained activation energies around 0.40 eV indicate that the conduction mechanism in the

studied BiFeO₃ film is associated to the first ionization of oxygen vacancies.

ACKNOWLEDGMENTS

This work was supported by the Fundação de Amparo à Pesquisa do Estado de São Paulo, FAPESP (Project 2017/13769-1); the Conselho Nacional de Desenvolvimento Científico e Tecnológico, CNPq (Grant 304604/2015-1); and the Coordenação de Aperfeiçoamento de Pessoal de Nível Superior, CAPES (CAPES-PRINT Project: 88887.310512/2018-00).

REFERENCES

- [1] J. Wang, J. B. Neaton, H. Zheng, V. Nagarajan, S. B. Ogale, B. Liu, D. Viehland, V. Vaithyanathan, D. G. Schlom, U. V. Waghmare, N. A. Spaldin, K. M. Rabe, M. Wuttig, and R. Ramesh, Epitaxial BiFeO₃ multiferroic thin film heterostructures, *Science*. **299**, 1719 (2003).
- [2] M. Bibes, and A. Barthelemy, Multiferroics: towards a magnetoelectric memory, *Nat. Mater.* **7** (6), 425 (2008).
- [3] Y.W. Li, Z.G. Hu, F.Y. Yue, P.X. Yang, Y.N. Qian, W.J. Cheng, X.M. Ma, J.H. Chu. Oxygen-vacancy-related dielectric relaxation in BiFeO₃ films grown by pulsed laser deposition. *J. Phys. D: Appl. Phys.* **2008**; **41**: 215403.
- [4] D.K. Pradhan, R.N.P. Choudhary, C. Rinaldi, R.S. Katiyar. Effect of Mn substitution on electrical and magnetic properties of Bi_{0.9}La_{0.1}FeO₃. *J. Appl. Phys.* **2009**; **106**: 024102.
- [5] S. Mukherjee, A. Srivastava, R. Gupta, A. Garg. Suppression of grain boundary relaxation in Zr-doped BiFeO₃ thin films. *J. Appl. Phys.* **2014**; **115**: 204102.
- [6] R. Schmidt, W. Eerenstein, T. Winiwiecki, F.D. Morrison, P.A. Midgley: Impedance spectroscopy of epitaxial multiferroic thin films. *Phys Rev B*. **2007**; **75**: 245111.
- [7] N. Ortega, A. Kumar, P. Bhattacharya, S.B. Majumder, R.S. Katiyar: Impedance spectroscopy of

- multiferroic $\text{PbZr}_x\text{Ti}_{1-x}\text{O}_3/\text{CoFe}_2\text{O}_4$. [*Phys. Rev. B.* **2008**; *77*: 014111.](#)
- [8] M. Vollmann, R. Hagenbeck, R. Waser. Grain-boundary defect chemistry of acceptor-doped titanates: Inversion layer and low-field conduction. [*J. Am. Ceram. Soc.* **1997**; *80*: 2301-2314.](#)
- [9] S. Song, F. Placido. The influence of phase probability distributions on impedance spectroscopy. [*J. Stat. Mech.: Theory Exp.* **2004**: P10018.](#)
- [10] E. J. Abram, D. C. Sinclair and A. R. West, [*J. Electroceram.*, **10**, 165-177 \(2003\).](#)
- [11] A. R. West, D. C. Sinclair and N. Hirose, [*J. Electroceram.*, **1**\(1\), 61-75 \(1997\).](#)
- [12] E. Barsoukov, J. R. Macdonald, Impedance spectroscopy: theory, experiment and applications, 3rd ed. John Wiley & Sons, New Jersey (2018)
- [13] W. Cao and R. Gerhardt, [*Solid State Ionics*, **42**, 213-221 \(1990\).](#)
- [14] S. Song and F. Placido, [*J. Stat. Mech.*, P10018 \(2004\).](#)
- [15] K. S. Cole and R. H. Cole, [*J. Chem. Phys.*, **9**, 341 \(1941\).](#)
- [16] A. K. Jonscher, Dielectric relaxation in solids, Chelsea Dielectric Press, London (1983)
- [17] Y-T. Chiang, P. B. Birnie and W. D. Kingery, Physical ceramics: principles for ceramic science and engineering, John Wiley & Sons, New Jersey (1996).
- [18] L. L. Hench and J. K. West, Principles of electronic ceramics, John Wiley & Sons, New Jersey (1990).
- [19] S. Hajra, S. Sahoo, R. Das, R.N.P. Choudhary, [*J. Alloy. Comp.* **750**, 507-514 \(2018\).](#)
- [20] C. G. Koops [*Phys. Rev.* **83**, 121 \(1951\).](#)
- [21] J. F. Araújo, J. Mendes Filho, F. E. A. Melo, F. V. Letelier and A. S. Chaves. [*Phys. Rev. B* **57**, 783-788 \(1998\).](#)
- [22] S. Mukherjee, A. Srivastava, R. Gupta and A. Garg, [*J. Appl. Phys.* **115**, 204102 \(2014\).](#)
- [23] H. Rahmouni, M. Smari, B. Cherif, E. Dhahri and K. Khirouni, [*Dalton Trans.* **44**, 10457-10466 \(2015\).](#)
- [24] J. Wu, and J. Wang, Ferroelectric and impedance behavior of La-and Ti-codoped BiFeO_3 thin films, [*J. Am Ceram Soc.* **93** \(9\), 2795 \(2010\).](#)
- [25] C. Ang, Z. Yu, and L. E. Cross, "Oxygen-Vacancy-Related Low-Frequency Dielectric Relaxation and Electrical Conduction in Bi: SrTiO_3 ," [*Phys. Rev. B.* **62**, 228 \(2000\).](#)

Mechanical and Solvent Transport Characteristics of Nitro and n-Butylphenyl Supported Poly(1,3,4-Oxadiazole)s

Nimisha Kaippamangalath^{1*}, Unnikrishnan Gopalakrishnanpanicker²,
Praveen C Ramamurthy³

¹Organic Nano Electronic Group, Department of Materials Engineering, Indian Institute of Science Bangalore, India

*Corresponding author, e-mail address: nimisha.24387@gmail.com

²Polymer Science and Technology Laboratory, Department of Chemistry, National Institute of Technology Calicut, India. e-mail address: unnig@nitc.ac.in

³Organic Nano Electronic Group, Department of Materials Engineering, Indian Institute of Science Bangalore, India. e-mail address: praveen@iisc.ac.in

Received 22 December 2019; accepted 4 March 2020; published online 10 March 2020

ABSTRACT

Examination of mechanical and solvent transport properties of π -conjugated polymers (PCPs), viz; poly(2-nitro-*p*-phenylene-1,3,4-oxadiazole) [PNPO], poly(*p*-phenylenevinylene-1,3,4-oxadiazole) [PPVO], poly(*p*-(nitrophenylene)vinylene-1,3,4-oxadiazole) [PNPVO], poly[(2-N,N'-dibutylaminophenyl)1,3,4-oxadiazole] [PNAPO], poly[pyridine(2-nitrophenyl)-1,3,4-oxadiazole] [PPNO] and poly[2-(*o*-nitrophenyl)-5-phenyl-1,3,4-oxadiazole] [PNPPO] has been done in flexible film form after blending them with poly(methylmethacrylate) or polystyrene. All six PCPs, in blended form, showed good mechanical properties with tensile strength in the range of 11.45 MPa - 22.89 MPa. Loading of TiO₂ nanoparticles onto selected polymer matrices has been found to contribute to a quantum enhancement in tensile properties. Solvent transport studies of blended polymer films and selected TiO₂ loaded matrices were carried out. Surfaces of films have been found to be predominantly hydrophobic ensuring a long service life for the appliances derived from them in moisture rich ambience.

1. INTRODUCTION

Study of mechanical and transport characteristics of macromolecules have been the key focus of many research programmes [1-2]. Mechanical properties of organic semiconductors are of critical importance during their bulk production and service period [3-4]. Despite the necessity of organic electronic materials to undergo large deformations in flexible, ultra-thin, and stretchable applications, many high-performance organic semiconductors are mechanically fragile.

Formation of composites of π -conjugated polymers (PCPs) with introduction of required

amount of compatible nanoparticles into polymer matrices is a powerful approach to obtain many balanced properties by exploiting the advantages of both PCPs and nanoparticles [5-6]. TiO₂ nanoparticles possess considerable mechanical strength and high surface area, and as a result, they have been widely introduced into many polymeric materials [7-8].

Synthesis, characterization and optical features of poly(2-nitro-*p*-phenylene-1,3,4-oxadiazole) [PNPO], poly(*p*-phenylenevinylene-1,3,4-oxadiazole) [PPVO], poly[*p*-(nitrophenylene)vinylene-1,3,4-oxadiazole] [PNPVO], poly[(2-N,N'-dibutylaminophenyl)1,3,4-oxadiazole] [PNAPO],

poly[pyridine (2-nitrophenyl) 1,3,4-oxadiazole] [PPNO], and poly[2-(*o*-nitrophenyl)-5-phenyl-1,3,4-oxadiazole] [PNPPO] have been reported by us elsewhere [9-11]. The mechanical and solvent transport features of these six conjugated polymers in the flexible film form have to be explored for device applications. Along with the optoelectrical features, the mechanical strength and solvent resistant behaviour of active layers has a critical role in determining better device performance in terms of optoelectronic device life span. Based on these evaluations, a systematic investigation has been done on mechanical and solvent transport features of conjugated polymers mentioned in this manuscript. The suitability of these six macromolecules for optoelectronic device fabrication has further been confirmed through this investigation.

2. MATERIALS AND METHODS

All materials used in this work were of analytical grade. Mechanical properties of polymer films were

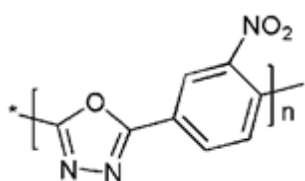
analyzed by universal testing machine. Samples in dumb bell shape (Gauge length = 2.5 mm) were drawn with a rate of 1 mm/min according to ASTM D-412. To study solvent resistant properties of blended films and composites, specimens of diameter 1.9 mm were prepared. Optical microscopic images were taken on Motic BA 300 optical microscope. Static contact angle measurements were performed using Drop Shape Analyzer (DSA) 100 (Kruss GmbH–Germany).

3. RESULTS AND DISCUSSIONS

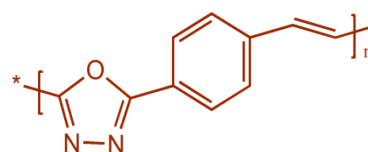
Polymer films of all six PCPs were fabricated by blending strategy. Details are given in our earlier reports [9-11]. The molecular structures of six PCPs studied in this manuscript are given in Figure 1.

3.1. Mechanical properties

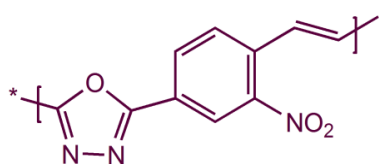
The mechanical properties of the blended polymer films with 2 wt% of PMMA/PS are summarized in Table 1. The tensile behaviour of the synthesized



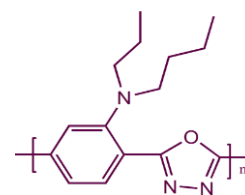
poly(2-nitro-*p*-phenylene-1,3,4-oxadiazole)



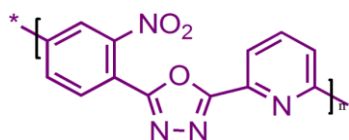
poly(*p*-phenylenevinylene-1,3,4-oxadiazole)



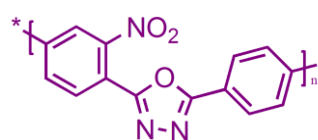
poly[*p*-(nitro phenylene)vinylene-1,3,4-oxadiazole]



poly[(2-*N,N'*-dibutyaminophenyl)1,3,4-oxadiazole]



poly[pyridine(2-nitrophenyl)1,3,4-oxadiazole]



poly [(2-(*o*-nitrophenyl)-5-phenyl-1,3,4-oxadiazole)]

Figure 1. Molecular structures of π -conjugated polymers.

PCPs is schematically illustrated in Figure 2. When a load is applied, the films (PCPs with PMMA/PS) show a yielding behaviour. This effectively helps them to accommodate the load being applied.

All films showed similar mechanical behaviour with respect to deformation under stress. Values of tensile strength are in the range of 11.45 MPa - 22.89 MPa (standard error +/-0.93128) and elongation at break in the range of 0.93 % - 3.05 %. The values are interestingly comparable or better than materials currently being used for fabrication of optoelectronic devices [12].

It has been observed that tensile properties of blends increase with increase in weight percentage of PMMA/PS from 2 wt% to 8 wt%. Typically, two

polymeric systems, PNPO and PPVO with PMMA/PS, were examined to see the dependence of weight percentage of PMMA/PS and results are presented in Figure 1a and b. After 4 wt% PMMA/PS loading, all macromolecular systems exhibited emission features with low intensity [11]. Tensile properties of polymer films with PS, in each case, have been found to be higher compared to that of corresponding PMMA samples; attributed to better π - π interactions between PCPs and PS. Interestingly, comparing mechanical properties reported for poly(oxadiazole) systems synthesized earlier, present polymers exhibit higher values indicating their suitability for device fabrication [13-14], in terms of product strength and service life.

Table 1. Tensile properties of blended polymer films with 2 wt% of PMMA/PS.

Polymer Films*	Tensile Strength (MPa)	Elongation at Break (%)
PNPO/PMMA	18.10	1.08
PNPO/PS	21.12	0.93
PPVO/PMMA	16.50	0.98
PPVO/PS	17.45	2.96
PNPVO/PMMA	19.20	3.05
PNPVO/PS	19.75	2.01
PNAPO/PMMA	11.45	1.98
PNAPO/PS	15.71	1.79
PPNO/PMMA	17.50	2.60
PPNO/PS	18.30	2.10
PNPPO/PMMA	22.15	1.34
PNPPO/PS	22.89	1.20

* with 2 wt% of PMMA/PS

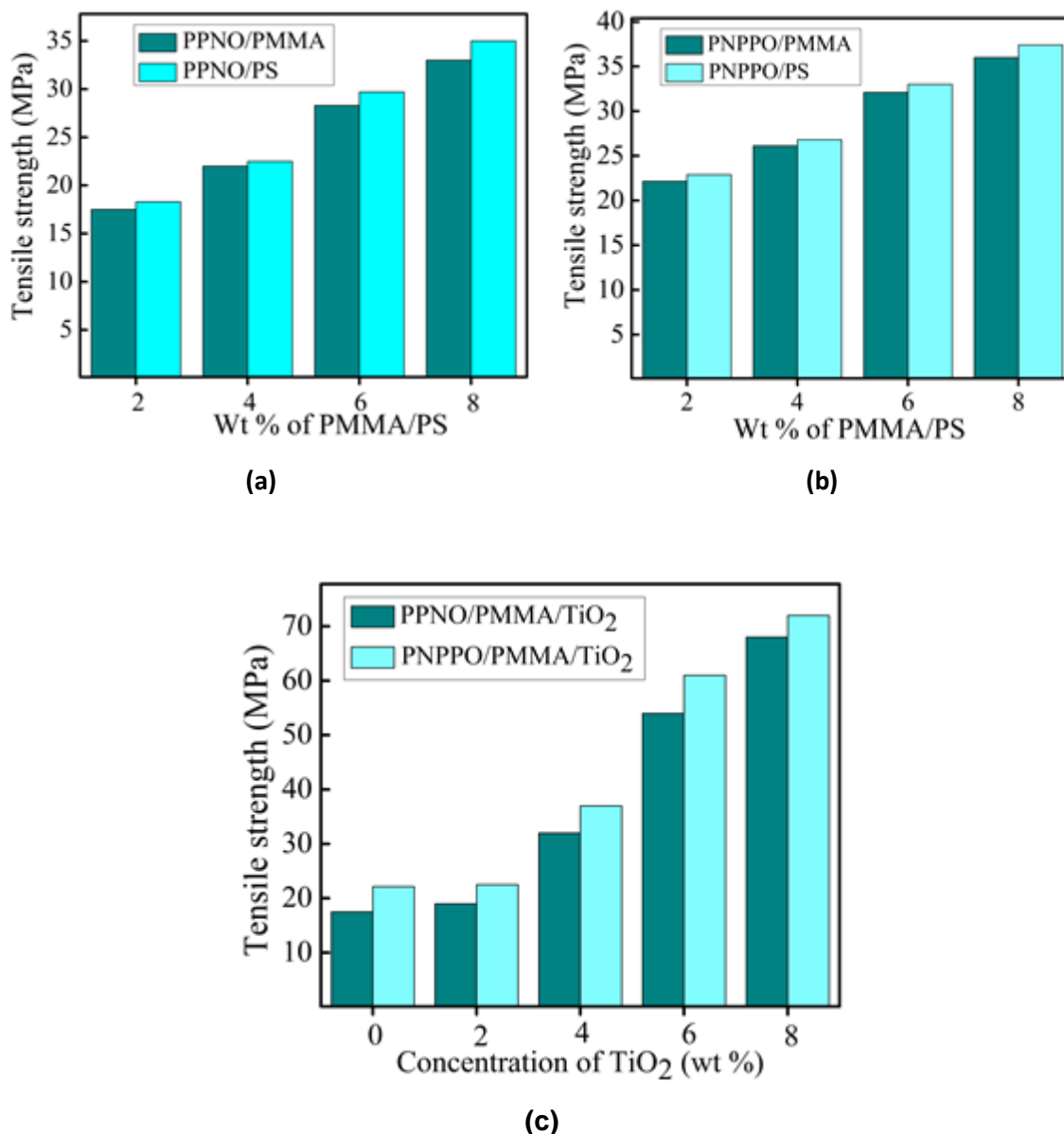


Figure 2. Mechanical properties of: (a) PPNO/PMMA or PS (b) PNPPO/PMMA or PS (c) PPNO/PNPPO nanocomposites with TiO₂.

Based on our previous publication [11], we have done a detailed study of mechanical features of PPNO/PNPPO nanocomposites with TiO₂ NPs in this manuscript. The loading of TiO₂ nanoparticles into polymer matrices, typically with PPNO and PNPPO, has been found to enhance the mechanical properties significantly (Figure 2c). Mechanical properties of nanocomposites largely depend on external load transfer efficiency

between nanofiller phase and matrix. Dispersion of TiO₂ NPs in polymer matrix reduces polymer-polymer interaction while increasing polymer-filler interactions. This physical reinforcement causes the system to resist applied forces, and thus tensile strength increases significantly.

Particle size and the surface area of filler play crucial role in reinforcement process. From the morphological evaluation, it has been confirmed

that spherical TiO₂ nanoparticles possess average size of 50 nm [11]. The nanosized particles have large surface area which offers effective interaction with matrices [15]. Total surface area of TiO₂ filler in PCPs is directly related to the amount or percentage of weight of TiO₂ dispersed in, which accounts for the observed elevation in mechanical properties with an increase in the amount of the filler (Figure 1c). Significant enhancement of tensile strength of polymer nanocomposites can also be due to anisotropic nature of TiO₂ nanoparticles; relates to its surface activity, and thus its interaction with host matrices [16, 17].

A theoretical model, proposed by Halpin-Tsai, has been adopted to compare tensile strength of composites of PPNO/PNPPO with TiO₂. According to this model, the relative tensile strength, RTS, can be expressed as [18].

$$RTS = \frac{\sigma_c}{\sigma_b} = \frac{1+\zeta\eta_T\phi_f}{1-\eta_T\phi_f} \quad (1)$$

where η_T is given by

$$\eta_T = \frac{R_T - 1}{R_T + \zeta} \quad (2)$$

and, σ_c and σ_b are tensile strength of the polymer composites and unfilled polymer systems, respectively. ϕ_f is volume fraction of TiO₂ in the

polymer matrices. R_T is filler tensile strength relative to that of polymer matrix and the aspect ratio.

The volume fraction of the nanofillers distributed throughout the matrix surface has a critical value in the reinforcement of tensile strength of nanocomposites. Although, there are different theories to explain the extent of reinforcement between matrix and nanofillers, the Halpin-Tsai model has better explained the relation between volume fraction of nanofiller, ϕ_f and tensile strength of the polymer composites, σ_c as shown in equation 1. It can be seen from Figure 3 that PNPO/PMMA/TiO₂ and PNPPO/PMMA/TiO₂ predominantly show positive deviations from theoretical predictions by Halpin-Tsai model. This observation is complementary to points discussed above, and is an indication of high filler-matrix interaction.

The tensile strength of the TiO₂ filled PPNO and PNPPO films showed an enhancement compared to their blended films with PMMA/PS. The homogeneous stress distribution in the PPNO/PNPPO based composites materials gives an improvement in strength. The theoretical values are higher than the experimental values. The increase in the deviation of theoretical values at higher TiO₂ loadings arises due to well uniform distribution of TiO₂ nanoparticles in case of low filler

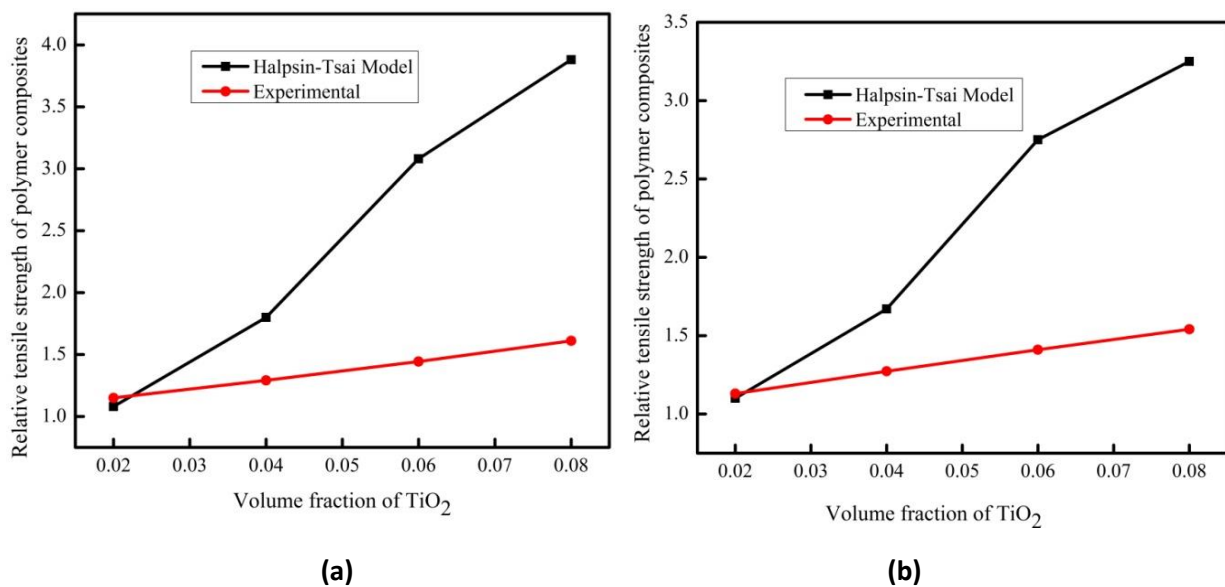


Figure 3. Comparison of relative tensile strengths of: (a) PPNO/PMMA/TiO₂ (b) PNPPO/PMMA/TiO₂.

loadings. Also, the Halpsin-Tsai model (Equation 1) does not account into the surface area or particle size of the TiO_2 distributed in PPNO and PNPPO surfaces.

3.2. OPTICAL MICROSCOPIC ANALYSIS

In an optical microscopic technique, the enhanced scattering of light in nanostructures, due to the coupling with the surface plasmon resonance (SPR), provides a powerful strategy for imaging the location of nanoparticles (NPs) in a matrix [19]. A light source (usually white light) was focused on the PPNO/PMMA or PNPPO/PMMA surface

containing strongly scattering TiO_2 NPs. The light frequencies correspond to SPR were reflected [20]. The light was then collected and imaged through a confocal microscope resulting in a colored image of the sample on a black background [21]. The wavelength of the light scattered depended on the shape and dimensions of TiO_2 NPs dispersed in the polymer matrix.

The optical microscopic images of the polymer films, PPNO/PMMA, PNPPO/PMMA and polymer nanocomposites, PPNO/PMMA/ TiO_2 , PNPPO/PMMA/ TiO_2 are shown in Figure 4. The images confirm the homogeneous film formation

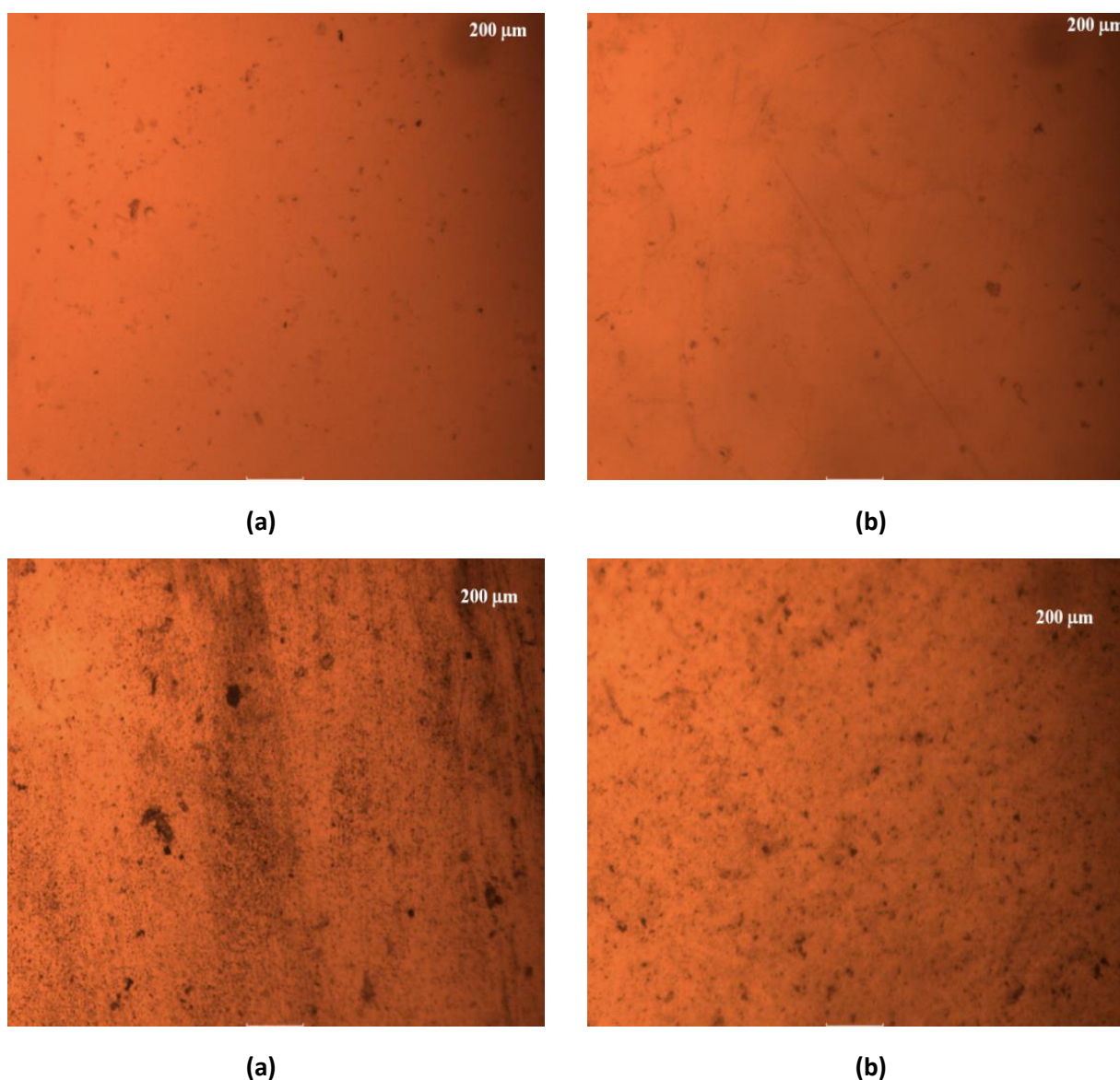


Figure 4. Optical images of: (a) PPNO/PMMA, (b) PNPPO/PMMA, (c) PPNO/PMMA/ TiO_2 and (d) PNPPO/PMMA/ TiO_2 (2 wt% TiO_2).

and the dispersion of TiO₂ nanoparticles within the matrix.

3.3. SOLVENT TRANSPORT PROPERTIES

Solvent transport properties of a PNPPPO blended film with PMMA in hexane, water and ethanol media are shown in Figure 5a. No dimensional change has been noted (practically, even after many months) in water. However, in strong organic solvents viz; hexane and ethanol, film has been found to absorb penetrant after sometime.

A small weight loss was noted both in hexane and ethanol (typically after 15 hours). A comparison study on transport behaviour of a typical nanocomposite, PNPPPO/PMMA/TiO₂ in hexane medium, has been illustrated in Figure 5b. In the case of NCs, the TiO₂ NPs acts superior barrier for transport of solvents. After a particular time, weight reduction of polymer blends and composites (curves pointing downward in the case of hexane and ethanol) is predominantly due to the solubility of PMMA.

An understanding of wetting behavior is very useful in the design and optimization of a wide-range of interface-sensitive optoelectronic devices and for conductive packaging material

applications. Water was selected as the working liquid for contact angle measurements to characterize the wetting properties of the fabricated polymer films. The contact angle of a liquid on a textured surface θ_r^w is a function of surface roughness and the equilibrium contact angle (θ_{flat}^e) on a flat substrate of the same material. This can be expressed as [22]:

$$\cos \theta_r^w = r \cos \theta_{flat}^e \quad (3)$$

where r is the surface roughness parameter.

In the case of nanocomposites polymer films, the contact angle of liquid drop on a heterogeneous substrate in an air medium can be expressed as [23]:

$$\cos \theta_r^{CB} = f_{sl} (1 + \cos \theta_{flat}^e) - 1 \quad (4)$$

where, f_{sl} is the contact area fraction parameter, i.e., the ratio of the liquid–solid contact area and the projected area of the drop base.

To measure the exact value of the contact angle, the drop-substrate contact was maintained for a longer time (> 1min) to allow the drop to spread without any additional force from the needle on the drop. It is obvious from Figure 6 that the all macromolecules and their blends exhibit nearly

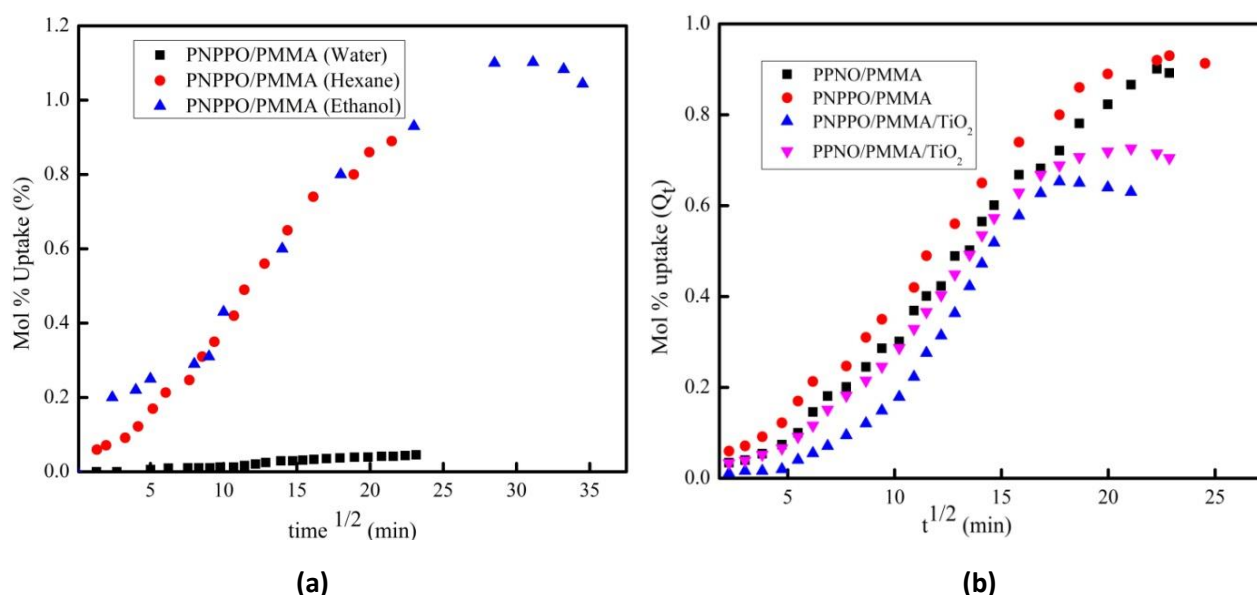


Figure 5. Solvent transport properties through (a) blended PNPPPO films (a) PNPPPO composites (2 wt % TiO₂) in hexane.

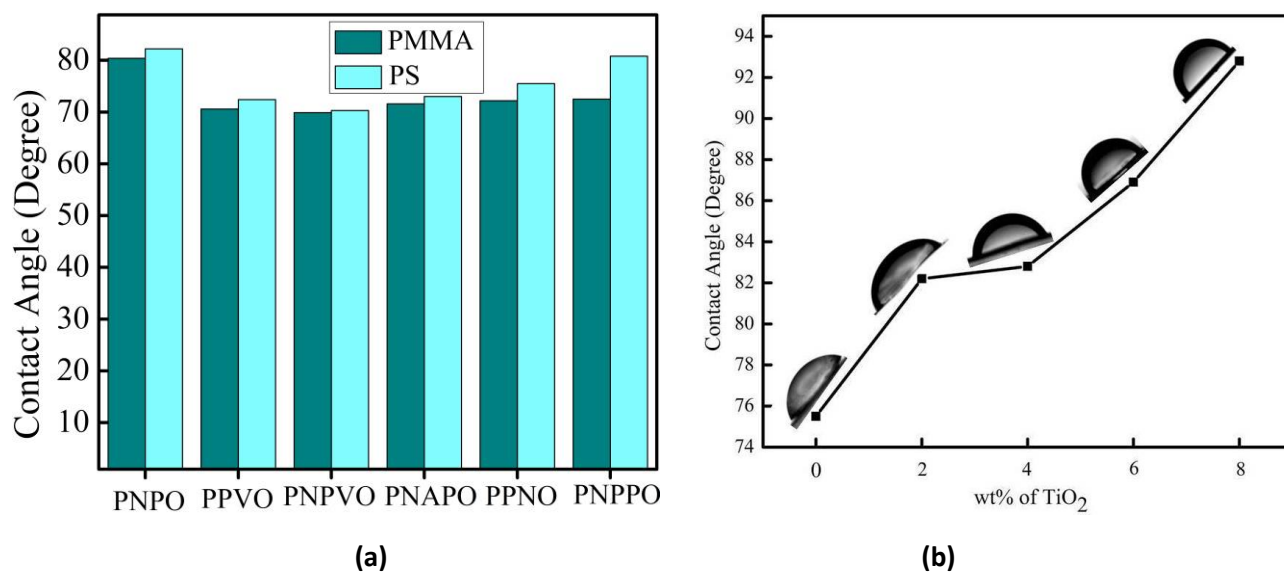


Figure 6.(a) Contact angles of polymer blends with PMMA/PS (b) Improvement of water repelling behaviour with increase in weight percentage of TiO₂ (PNPPO/PMMA/TiO₂).

same contact angles. These values are near to the values of typical hydrophobic matrices. In all cases, the blended polymer samples with PS showed higher contact angle values than that with PMMA; resulting from the more hydrophobic nature of PS.

The water repelling behaviour of composites has also been studied with the variation of wt % of TiO₂ NPs as shown in Figure 6b. A gradual improvement in the contact angle values with increase in the wt % of TiO₂ NPs has been observed. This is attributed to the poor wetting behavior of TiO₂ nanoparticles to a range of solvents (mostly from the polar protic solvent family) [24-26]. It is well understood that the chemical heterogeneity and surface topography significantly influence the wetting characteristics of a substrate [26].

4. CONCLUSIONS

A systematic investigation on the physical properties viz; mechanical and solvent transport of the six macromolecules, poly(2-nitro-*p*-phenylene-1, 3, 4-oxadiazole) [PNPO], poly(*p*-phenylenevinylene-1, 3, 4-oxadiazole) [PPVO], poly[*p*-(nitrophenylene)vinylene-1,3,4-oxadiazole] [PNPVO], poly[(2-N,N'-dibutylaminophenyl)1, 3, 4-oxadiazole] [PNAPO], poly[pyridine(2-nitrophenyl)-

1,3,4-oxadiazole] [PPNO], and poly[2-(*o*-nitrophenyl)-5-phenyl-1,3, 4-oxadiazole] [PNPPO] has been done in the blended and composites forms. The tensile strength values and elongation at break of the polymer films are interestingly comparable to that of the materials used as active layers in optoelectronics. The films exhibited good resistance to water. Contact angle measurements confirmed their dominant hydrophobicity. Observations presented in this work are complementary to the optical features of the new macromolecules in view of their possible utilization in optoelectronic devices and as conducting packaging materials.

ACKNOWLEDGMENTS

NK acknowledge CSIR, New Delhi, India and KSCSTE Postdoctoral fellowship.

REFERENCES

- [1] Y.-S. Lee, G.-D. Sim, J.-S. Bae, J.-Y. Kim and S.-B. Lee, *Mater. Lett.* **193**, 81-84 (2017).
- [2] K. Hamad, M. Kaseem, F. Deri and Y. G. Ko, *Mater. Lett.* **164**, 409-412 (2016).
- [3] A. D. Printz, S. Savagatrup, T. N. Purdy and D. J. Lipomi, *RSC Adv.* **4**, 13635-13643 (2014).
- [4] Y. Cao, P. Smith and A. J. Heeger, *Polymer* **32**, 1210-1218 (1991).

- [5] A. C. Balazs, T. Emrick and T. P. Russell, [Science](#)**314**, 1107-1110 (2006).
- [6] N. Chehata, A. Ltaief, R. Bkakri and E. Beyou, [Mater. Lett.](#) **121**, 227-230 (2014).
- [7] H. Zhang, J. Huang, X. Lin and J. Qu, [RSC Adv.](#) **5**, 4639-4647 (2015).
- [8] X. Sui, Y. Chu and C. Liu, [Mater. Lett.](#) **58**, 1255-1259 (2004).
- [9] N. Kaippamangalath, U. Gopalakrishnanpanicker, E. Shiju and K. Chandrasekharan, [J. Mater. Sci.](#)**51**, 4748-4761 (2016).
- [10] N. Kaippamangalath and U. Gopalakrishnanpanicker, [Polym. Int.](#) **65**, 1221-1231 (2016).
- [11] N. Kaippamangalath, U. Gopalakrishnanpanicker, E. Shiju and K. Chandrasekharan, [RSC. Adv.](#) **6**, 115132-115144 (2016).
- [12] X. Lu, Z. Zhang, H. Li, X. Sun and H. Peng, [J. Mater. Chem.](#) **A2**, 17272-17280 (2014).
- [13] M. D. Iosip, M. Bruma and P. Muller, [Eur. Polym. J.](#)**39**, 2011-2021 (2003).
- [14] C. Hamciuc, M. Klapper and T. Pakula, [Polym. Bull.](#) **47**, 1-8 (2001).
- [15] G. Kaur, R. Adhikari, M. Bown and P. Gunatillake, [RSC Adv.](#) **5**, 37553-37567 (2015).
- [16] M. Wojtaś, D. V. Karpinsky, M. V. Silibin, S. A. Gavrilov, A. V. Sysa and K. N. Nekludov, [Polym. Test.](#) **60**, 326-332 (2016).
- [17] M. Wojtas, D. V. Karpinsky, M. V. Silibin, S. A. Gavrilov, A. V. Sysa, K. N. Nekludov and S. V. Dubkov, [Polym. Test.](#) **71**, 296-300 (2018).
- [18] J. C. Halpin and J. L. Kardos, [Polym. Eng. Sci.](#) **16**, 344-352 (1976).
- [19] X. Huang, P. K. Jain, I. H. El-Sayed and M. A. El-Sayed, [Nanomedicine](#)**2**, 681-693 (2007).
- [20] P. K. Jain, X. Huang, I. H. El-Sayed and M. A. El-Sayed, [Acc. Chem. Res.](#) **41**, 1578-1586 (2008).
- [21] S. K. Brauman, [J. Polym. Sci.](#) **B26**, 1159-1171 (1988).
- [22] A. B. D. Cassie and S. Baxter, [Trans. Faraday Soc.](#) **40**, 546-550 (1944).
- [23] Kim, K. Noh, C. Choi, J. Khamwannah, D. Villwock and S. Jin, [Langmuir](#)**2011**, **27**, 10191-10196 (2011).
- [24] E. Balaur, J. M. Macak, H. Tsuchiya and P. Schmuki, [J. Mater. Chem.](#)**15**, 4488-4491 (2005).
- [25] S. Barthwal, Y. S. Kim and S.-H. Lim, [J. Colloid Interface Sci.](#) **400**, 123-129 (2013).
- [26] S. Farsinezhad, P. R. Waghmare, B. D. Wiltshire, H. Sharma, S. Amiri, S. K. Mitra and K. Shankar, [RSC Adv.](#) **4**, 33587-33598 (2014).

Sizing electrode and its effect on performance of a microactuator

Mohamed Ahmed ESHAG^{1,2,3}, Musaab ZAROG^{4*}

¹ School of Electrical Engineering, Southwest Jiaotong University, Chengdu, 610031, China

² School of Mechanical Engineering, Faculty of Engineering, Sudan University of Sciences and Technology, P.O. Box.407, Khartoum, Sudan

³PLOP Department, Petro-Energy E&P Co. Ltd, PDOC & PE Tower, Alsunut Area, Almogran, Khartoum, Sudan

⁴ Department of Mechanical and Industrial Engineering, College of Engineering, Sultan Qaboos University, P.O. Box 33, Al-Khod, Muscat, 123, Oman

*Corresponding author, e-mail address: musaabh@squ.edu.om

Received 22 January 2020; accepted 4 March 2020; published online 10 March 2020

ABSTRACT

The vibration amplitude and its frequency are the main factors that affect the performance of resonating microactuators and microsensors. Electrostatic and piezoelectric actuation/sensing are very common methods used to design Microelectromechanical Systems (MEMS). Both methods require adding electrode layer for detection or actuation purposes which is normally very small in dimension and therefore have low effect on the performance of MEMS device. In some cases, even a small shift in the vibration resonance frequency of the device or its amplitude of vibration can highly affect the device performance. This work investigates the effect of sizing electrode on the performance of electrostatically actuated MEMS device. Electrode length was varied from fully covering the actuator layer to covering 10% only. ANSYS finite element was used as a simulation tool.

1. INTRODUCTION

MEMS resonators are the key players in most of the MEMS sensors and actuators. Electrostatic actuation is most commonly used method of actuation compared to other alternative methods (e.g. electrothermal and piezoelectric) and this is mainly due to the low power consumption and ability to very high resonance frequencies [1, and 2]. Electrode layers are used to apply electrostatic voltage to the actuated resonators. For cantilever resonator, a top layer of electrode is deposited to conduct voltage. The electrode characteristics (geometrical dimensions and elastic parameters) will influence the performance of the resonating structure [3]. On the other hand, the deposited electrode material might have undesirable mechanical and electronic properties compared to resonator device. Reducing the electrode length will reduce their effect but at the same time this will

affect the active area for electrostatic actuation which may require high voltage to be applied. Effect of reshaping the metal electrode as well as changing the thickness, on the functionality of the resonators, were investigated in the literature [4,5, 6 and 7]. This work aims to investigate the effect of electrode length on the amplitude of electrostatically actuated microcantilever.

2. MODEL OF AN ELECTROSTATIC ACTUATOR

Electrostatic actuator, under investigation, consist of four main parts: silicon base layer ($200 \times 2 \times 20 \mu\text{m}^3$), isolator layer silicon dioxide ($50 \times 3 \times 20 \mu\text{m}^3$), silicon actuator layer ($200 \times 2 \times 20 \mu\text{m}^3$), and copper pad layer ($200 \times 2 \times 20 \mu\text{m}^3$). The device layout, which was modelled in finite element (FE) software (ANSYS v.15), is shown in Figure.1. The properties of material used are presented in Table.1.

Table 1. Material properties.

Properties material	Elastic Modulus (MPa)	Poisson's Ratio (PR)	Density (Kg/ μm^3)	Thermal Expansion Coefficient $t(\alpha), 1/C$	Thermal Conductivity (K), $\text{pW}/\mu\text{m}^{\circ}\text{C}$	Resistivity (R) (ohm-m)
Si	185×10^3	0.28	23×10^{-15}	2.33×10^{-6}	157×10^6	6.4×10^2
SiO ₂	73×10^3	0.23	22.7×10^{-15}	0.5×10^{-6}	1.4×10^6	1×10^{13}
Cu	110×10^3	0.34	89×10^{-15}	16.56×10^{-6}	393×10^6	1.72×10^{-8}

To verify the ANSYS model, natural frequency was calculated and compared with the value obtained from FEM model using the following equation [8]:

$$f = 0.16 \frac{t}{l^2} \sqrt{\frac{E}{\rho}}$$

Where, f =Natural frequency (Hz), E = Elasticity modulus (Pa), ρ = Density (kg/m^3), t = thickness (m), li =Electrode length over cantilever for different (i) length, $n=2$ (the ratio of two areas), since the cantilever is made of actuator and pad layer the equivalent Young's modulus was calculated as follows:

$$E_{eq} = \frac{\sum l}{\sum_{i=1}^2 \frac{li}{Ei}} = 137.966 \times 10^9 \text{ N}/\text{m}^2$$

And the equivalent density was calculated to be $5600 \text{ kg}/\text{m}^3$

$$f = 0.16 \times \frac{0.004 \times 10^{-3}}{[0.2 \times 10^{-3}]^2} \times \sqrt{\frac{137.966 \times 10^9}{5600}} = 79 \text{ KHz}$$

The calculated value of resonance frequency (79 kHz) is close to the value obtained by ANSYS (79 kHz). Since the aim of this work is to investigate the effect of the length of pad layer (electrode), the resonance frequency was calculated for different

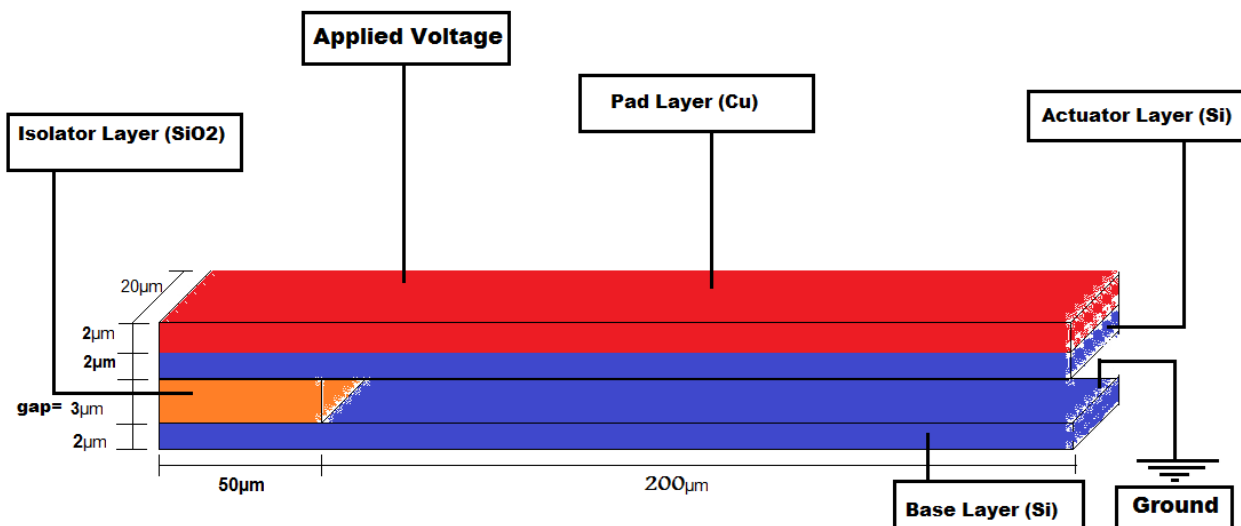


Figure 1. Geometry for electrostatic microcantilever.

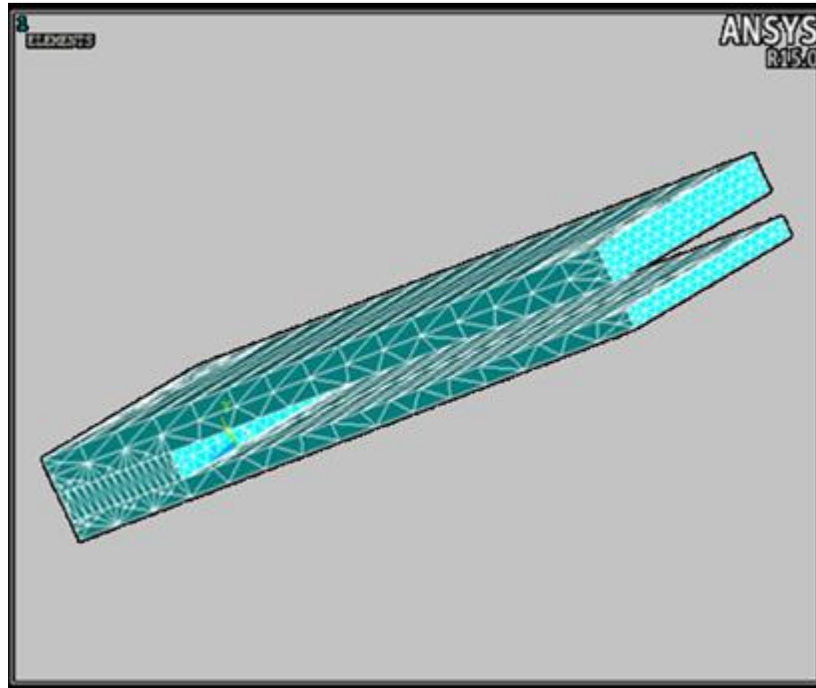


Figure 2. ANSYS meshing of the micro-cantilever device.

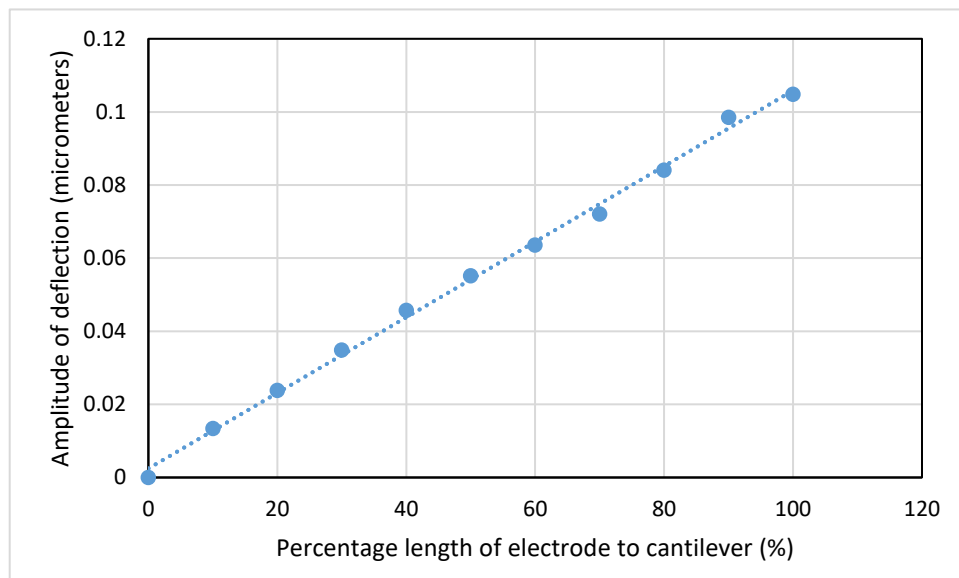


Figure 3. Linear relation between the amplitude of deflection and electrode geometry (for 10mV applied voltage).

lengths of electrodes as shown in Table.2. The large errors in the ANSYS calculated frequencies could be related to the meshing errors.

The model was developed and simulated in ANSYS (R.15). Attributed mesh was carried out, were each layer of actuator was meshed

separately shown in Figure.2. Solid227 has been used as element type for all layers. Structural loads were applied to fix the end of the cantilever. Electrical loads were also applied for electrical actuation with electrodes.

2. RESULTS AND DISCUSSION

The applied voltage was then varied from 0 to 200 mV while reducing the size (length) of the electrode layer 100% (when it is fully covers the actuator layer) to 10% of the actuator layer. The results are shown in Figure.2. Although some of the maximum deflection values exceed the electrostatic gap value (which indicates that the actuator will hit the

base layer), it is acceptable since it is not meant to mimic a real case. Alternatively, we can consider the values of deflection that are below 3 μm or even below the pull in gap. If the geometry of the model is modified, larger gap can be specified, and we could still obtain same relations about the effect of the electrode length.

The expected linear relation between the amplitude of deflection and electrode geometry (for 10mV applied voltage) can be seen in Figure.3.

Investigating the dynamic behavior of an electrostatically actuated cantilever, based on simple plate theory, shows that the amplitude of deflection is proportional to the square of applied voltage. The electrostatic force (F) generated for

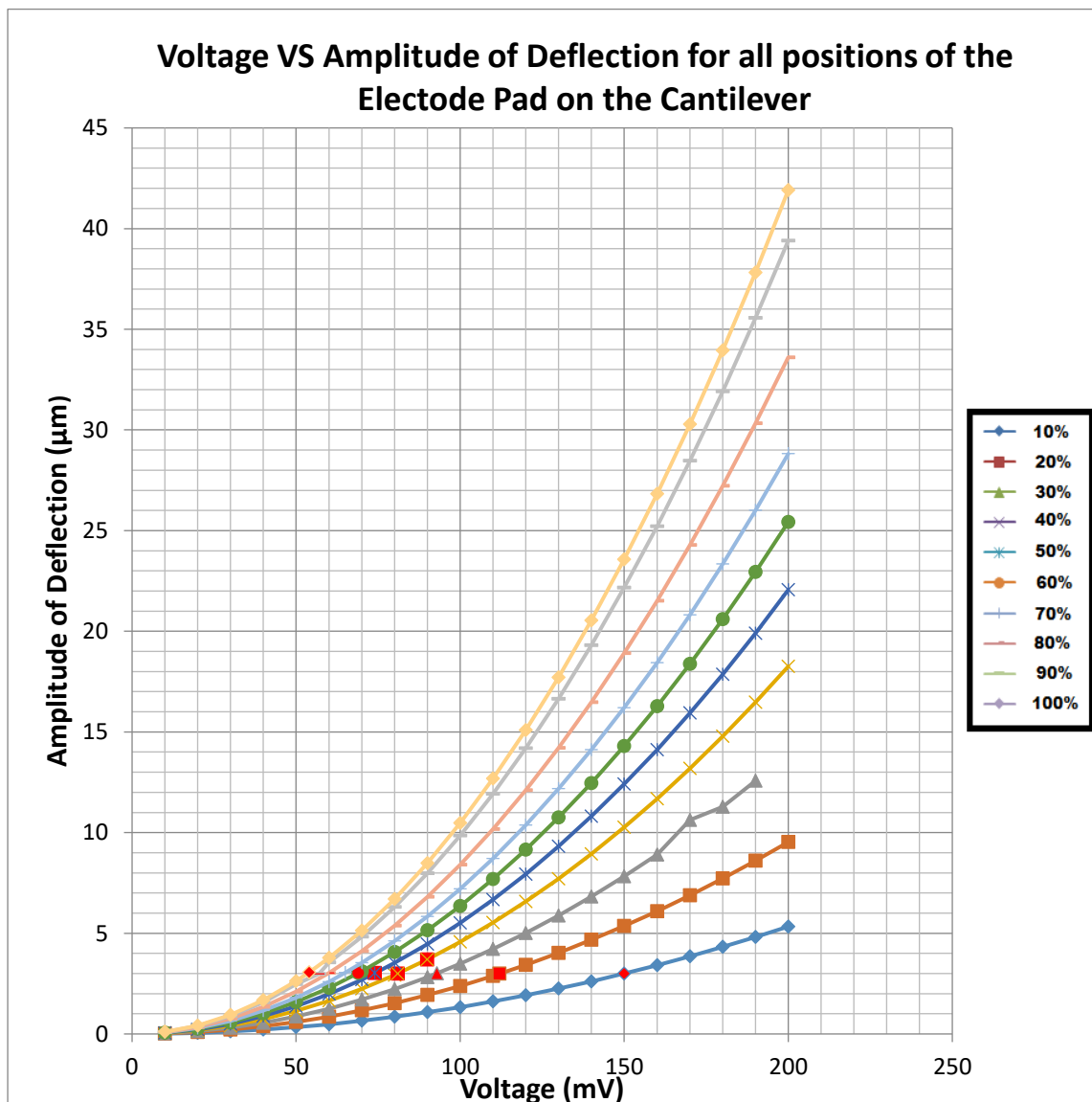


Figure 4. Voltage VS Amplitude of deflection at all positions of electrode Pad on the Cantilever.

Table 2. Natural frequency for different electrode lengths.

% of cantilever covered with Electrode pad	Electrode Length(μm) (li)	Natural Frequency(KHz) By ANSYS	Natural Frequency (KHz) By Calculation	Error for Natural Frequency (%)
100	200	78.1238	79.4167	1.628
90	180	100.799	98.708	2.074
80	160	145.563	125.879	13.52
70	140	149.002	165.837	10.15
60	120	231.653	227.965	1.59
50	100	328.204	332.048	1.16
40	80	556.157	525.827	5.453

simple parallel plates follows this relation generated by applying a voltage V is [9];

$$F = \frac{V^2 \epsilon_0 A}{2d^2} = kZ$$

where ϵ_0 is the permittivity in vacuum, d is the gap between the two electrodes, A is the area of one capacitor plate, k is the spring constant of the cantilever and Z is the amplitude of deflection due to V.

The results in Figure.4 confirms that the amplitude of deflection is not linearly proportional to the applied voltage.

4. CONCLUSIONS

The effect of electrode geometrical dimensions (length) on the performance of the resonating structure was investigated. Sizing the electrode length doesn't only affect the natural frequency of the structure but it also affect the amplitude of deflection and the voltage necessary to achieve certain deflection level. The results show that the amplitude of deflection may decrease significantly as a result of reducing the size of electrode. For example, at 200 mV, reducing the electrode length to one tenth reduces the amplitude of deflection

almost eight times. The authors recommend that the presented finite element analysis can be further developed to address issues like; stress-strain analysis, and nonlinear mechanical behavior inherent in the materials used.

REFERENCES

- [1] A. Abdallah, A. Ishag, S. Osman, M. Yousif, and M.Hassan, International Journal of Mechatronics, Electrical and Computer Technology, 4(10), (2014)
- [2] A. Atia, M.Ibrahim, O. Abdlgbar, and M. Hassan, [International Conference on Computing, Electrical and Electronics Engineering, Corinthia Hotel, Khartoum, 26 Aug - 28 Aug \(2013\).](#)
- [3] M. Brissaud, S. Ledren, and P. Gonnard, [Journal of micromechanics and microengineering, 13\(6\), 832–844. \(2003\).](#)
- [4] J.-H., Kuang, and C.-J. Chen, [International Journal of Mechanical Sciences, 47\(8\), pp. 1172–1190. \(2005\).](#)
- [5] Y. Yuan, H. Du, X. Xia, and Y. Wong, [Smart Materials and Structures, 23\(9\), 095005 \(10pp\) \(2014\).](#)
- [6] C.- C.Lee, , Q.Guo, G. Z.Cao, & I. Y. Shen, [Sensors and Actuators A: Physical, 147\(1\), 279-289 \(2008\).](#)
- [7] M. Ghayesh, H. Farokhi, and G. Alici, [International Journal of Mechanical Sciences, 103, 247–264, \(2015\).](#)
- [8] N. Maluf and K. Williams,"An Introduction to Microelectromechanical Systems Engineering", Second Edition,(2004)
- [9] L. Jiang et al., [Microelectronic Engineering 78–79, 106-111 \(2005\).](#)

Growth and spectral characteristics of single crystal layer of $KY(WO_4)_2$ doped with Ho^{3+} ions

S. Guretsky¹, D. Karpinsky^{1,*}, I. Kolesova¹, A. Kravtsov¹, D. Zhaludkevich¹,
S. Ozelik², O. Dernovich³, N. Kuleshov³

¹Scientific and Practical Materials Research Center NAS Belarus, Minsk, Belarus,

*Corresponding author, e-mail address: crystal2@ifftp.bas-net.by

² Photonics Application & Research Center, Gazi University, Ankara, Turkey

³Belarusian National Technical University, Minsk, Belarus

Received 24 January 2020; accepted 3 March 2020; published online 10 March 2020

ABSTRACT

We report on the growth and the characterization of Ho^{3+} doped $KY(WO_4)_2$ layers having high structural homogeneity and optical quality. The epitaxial layer of $Ho(5.0 \text{ at.}\%):KGd_{0.028}Yb_{0.047}Y_{0.875}(WO_4)_2$ with a thickness of 140 μm was fabricated by liquid phase epitaxy. The layer can be used as gain medium of planar waveguide lasers, emitting in the spectral range of about 2 μm .

1. INTRODUCTION

The infrared lasers operating in the eye-safe spectral range near 2 μm are used for free space applications, medical treatments, material processing, as well as a pump source for optical parametric oscillators [1-3]. Traditionally materials in this spectral region are Tm^{3+} - and Ho^{3+} -doped media. The absorption of Tm^{3+} at 800 nm makes possible an efficient pumping of its $^3H_6 \rightarrow ^3H_4$ transition by commercially available high power AlGaAs diode lasers. Cross-relaxation process ($^3H_6, ^3H_4 \rightarrow ^3F_4, ^3F_4$) leads to achieving a quantum efficiency well above unity [4]. Other attractions of Tm -doped lasers include its wide continuous wavelength tunable range [5]. Diode-pumped Tm lasers can be used for direct excitation of the upper laser level of Ho ions ($^5I_8 \rightarrow ^5I_7$). Such in-band pumping minimizes the quantum-defect-induced heat generation and reduces up-conversion processes probability.

In this work, we study a single-crystal layer of potassium tungstate having mixed chemical composition doped with trivalent holmium ions to use it as the gain medium for a waveguide laser under in-band laser pumping. Potassium double tungstate crystals, $KRe(WO_4)_2$ ($Re = Gd, Y, Lu$), serve as excellent hosts for trivalent rare-earth ions and are considered to be promising materials for waveguide lasers because of their high refractive indices [6]; large transition cross-sections [7]; long inter-ionic distance [8], allowing for large doping concentrations.

The gain medium of the waveguide planar lasers is a thin layer of active substance with a higher refractive index as compared to surrounding material. This makes it possible to localize the pump and generation radiation in a narrow spatial region with a size of several tens or hundreds of microns throughout the entire length of the waveguide, which leads to a high spatial consistency of the resonator and pump modes. That in turn provides high gains, low generation thresholds and greater resistance to thermal

effects. Active waveguide structures allow to create integrated high-performance optical systems for data processing.

2. EXPERIMENTAL

Growth of a single crystal layer of potassium-yttrium tungstate, co-doped with optically inert ions of gadolinium and ytterbium (under resonant pumping conditions) and an active holmium ion, was produced by liquid phase epitaxy on a substrate of $KY(WO_4)_2$ crystal, using a solution of $Ho(5at\%):KGd_{0.028}Yb_{0.047}Y_{0.875}(WO_4)_2$, in melted $K_2W_2O_7$, which had lateral dimensions of 10x10 mm and 2 mm thickness along b-axis. As the growth process was performed at quite low temperature (900-920°C) a viscosity of solution-melt was decreased via adjusting of a concentration of K_2O . The growth was performed in excess of K_2O estimated as 10-12 wt.% of the total mass of the solution-melt, thickness of the film was about 140 μm , concentration of Ho^{3+} ions ~5.0 at.%. The process of crystallization in the method of liquid-phase epitaxy is carried out due to the supersaturation of the solution-melt near the interface line in central near-surface area. The growth was carried out at a temperature of 900-920 °C, the substrate rotation speed was about 30-40 cycles per minute. The solution-melt was heated in a crucible above the saturation temperature by 30–50 °C and homogenized during 12 hours. Further, the temperature dropped by 1.5-2.5 °C below the saturation temperature and the substrate growth was performed to a planned thickness.

The obtained sample was cut along the axes of the optical indicatrix N_m and N_g and polished to a layer thickness of 140 μm (along b-axis). A photograph of the layer cross-section, obtained with a microscope Polam RP-1 (LOMO) using a CCD camera is shown in Figure 1. The grown layer is characterized by the absence of inhomogeneities, cracks and significant defects.

3. RESULTS AND DISCUSSION

X-ray structural analysis of the epitaxial layer, performed based on the data obtained with Bruker D2 diffractometer, has confirmed high structural quality of the layer. As the diffraction measurements were done on a bulk oriented sample, the diffraction spectrum contains only reflections from planes (0k0). The determined value of the b-parameter of the crystal lattice of the layer is 10.341 Å and the mismatch with the b-parameter of the substrate is 0.009%. This value is one order of magnitude smaller than the limit which determines a growing of the layers free of cracks [9].

The concentration of the rare-earth elements in the epitaxial layer was determined by energy-dispersive X-ray spectroscopy. The concentration of holmium ions Ho^{3+} was 5.0 at.%, and stoichiometric formula is $Ho_{0.05}:KGd_{0.028}Yb_{0.047}Y_{0.875}(WO_4)_2$.

Absorption spectrum of the sample was obtained using Fourier spectrometer (Vertex 70, Bruker) with a spectral resolution of 1 cm^{-1} in the spectral range of 1800-2200 nm for the radiation

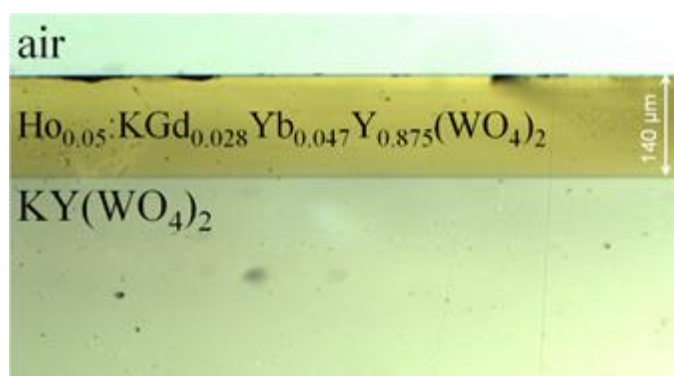


Figure 1. Photo of a single crystal layer activated by holmium ions grown on $KY(WO_4)_2$ crystal.

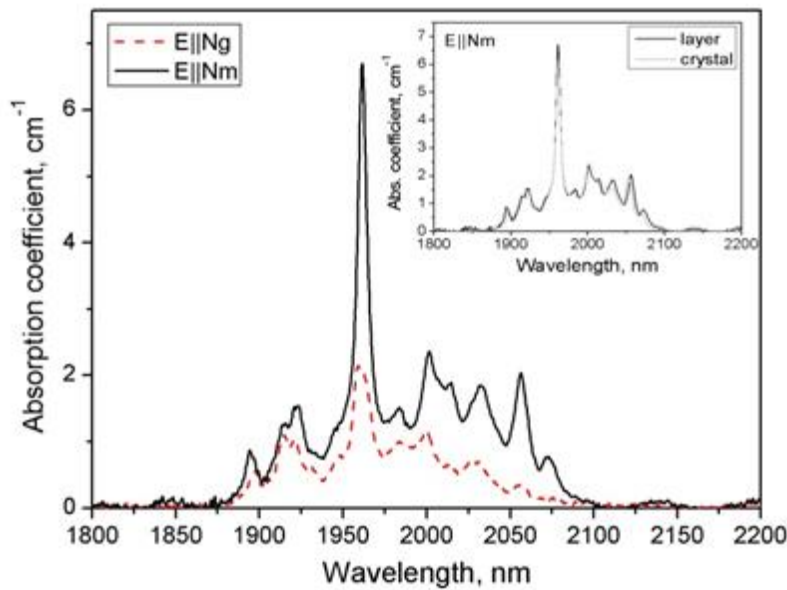


Figure 2. Absorption spectrum of a single crystal layer $\text{Ho}_{0.05}:\text{KGd}_{0.028}\text{Yb}_{0.047}\text{Y}_{0.875}(\text{WO}_4)_2$ in the range of $2 \mu\text{m}$.

polarized along the axes of optical indicatrix N_m and N_g (Figure 2).

The absorption spectrum is characterized by significant anisotropy for the radiation with different polarizations and the spectrum is identical to the spectrum of a bulk crystal (Figure 2 on the inset).

The luminescence spectrum of the sample under InGaAs laser diode (975 nm) excitation was

dispersed with MDR-23 monochromator and registered with InGaAs PIN photodiode (G5853 Hamamatsu) connected to a lock-in amplifier (SR810 Stanford Research Systems). The measured spectrum is shown in Figure 3 with the similar spectrum of the bulk Ho:KYW crystal. The polarization of radiation is indicated in the Figure.

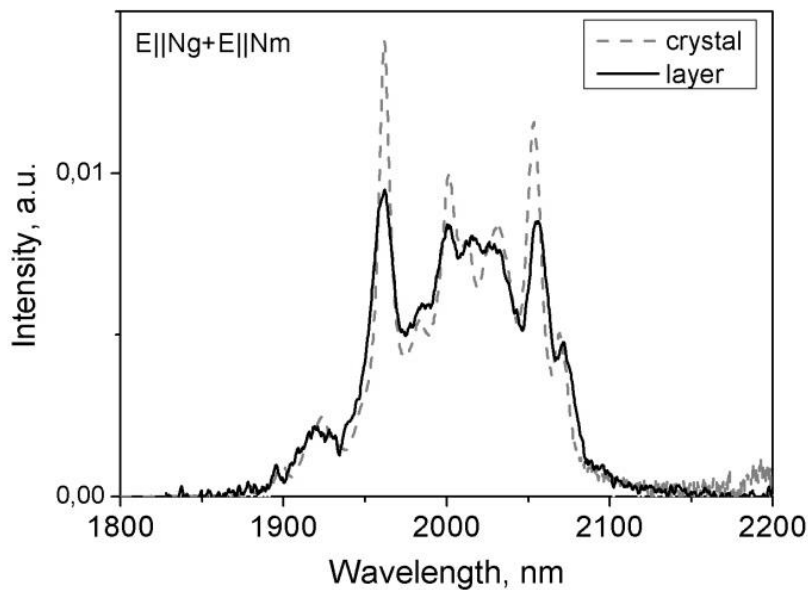


Figure 3. Luminescence spectra of the $\text{Ho}_{0.05}:\text{KGd}_{0.028}\text{Yb}_{0.047}\text{Y}_{0.875}(\text{WO}_4)_2$ layer and the bulk Ho:KYW crystal.

Some inconsistency between the indicated spectra is caused by insufficient resolution of the measured layer spectrum due to the weak luminescence signal. This is explained by a non-optimal excitation scheme through the energy transfer from the $^2F_{5/2}$ state of ytterbium ions to holmium ions.

4. CONCLUSIONS

Thus, high optical quality Ho(5at.%) -doped $\text{KGd}_{0.028}\text{Yb}_{0.047}\text{Y}_{0.875}(\text{WO}_4)_2$ epitaxial layer with 140 μm thickness along b-axis was obtained by liquid phase epitaxy technique. The sample is characterized by high optical and structural quality and can be used as a gain medium of planar

waveguide lasers, emitting in the spectral range of about 2 μm .

REFERENCES

- [1] B. Walsh, [Laser Physics, v.19, 4, 855-866, \(2009\).](#)
- [2] I. Sorokina, *Berlin-Heidelberg: Springer-Verlag*, 558, (2003).
- [3] A. Godart, [Comptes Rendus Physique, 8, 1100-1128, \(2007\).](#)
- [4] O. Silvestre et al., [Appl. Phys. B, 87, 707, \(2007\).](#)
- [5] O. Dernovich et. al., *Devices and Methods of Measurements*, v. 7, 2, 122-128, (2016).
- [6] A. Kaminskii et.al., [Crystallogr. Rep. 46, 665-672, \(2001\).](#)
- [7] N. Kuleshov et.al., [Opt. Lett., 22, 1317-1319, \(1997\).](#)
- [8] M. Pujol et. al., [J. Appl. Crystallogr., 35, 108-112, \(2002\).](#)
- [9] S. Aravazhi et.al., [Appl. Phys. B, 111, 433-446, \(2013\).](#)

Nanomaterials Science & Engineering (NMS&E), Vol.2, No.1, 2020

**Department of Mechanical Engineering
University of Aveiro
Aveiro 3810-193
Portugal**

<https://proa.ua.pt/index.php/nmse/>

ISSN: 2184-7002